MOLECULAR DYNAMICS SIMULATION AND NEUTRON SCATTERING STUDIES OF NONAQUEOUS ELECTROLYTE SOLUTIONS

BY

ZHIXIA LI

THESIS

Submitted in partial fulfillment of the requirements
for the degree of Master of Science in Nuclear, Plasma, and Radiological Engineering
in the Graduate College of the
University of Illinois at Urbana-Champaign, 2018

Urbana, Illinois

Master's Committee:

Associate Professor Yang Zhang, Adviser
Associate Professor Tomasz Kozlowski

Abstract

Nonaqueous electrolyte solutions have been widely investigated for a variety of applications due to their outstanding properties such as high conductivity and excellent stability. However, establishment of predictive models for nonaqueous electrolytes remains challenging. Molecular packing and clustering effects in complex liquid systems such as redox-active electrolyte solutions are still poorly understood especially at high concentrations. Here, neutron scattering is used to probe the dynamics at molecular level in nonaqueous organic electrolytes over a wide temperature range. Two model solution systems were chosen: one containing highly symmetric electrolyte molecules prone to crystallization and one containing a de-symmetrized liquid electrolyte preferring disordered states. In the latter case, complete supercooling (preservation of a disordered state below the melting point without crystallization) was observed to very low temperatures at high concentrations. However, upon heating, localized cold crystallization occurs, leading to a burst nucleation of microcrystalline solids within liquid-like components. Our findings indicate the clustering in these materials and point out limits in solvation and molecular crowding in concentrated nonaqueous electrolyte fluids. Although molecular dynamics (MD) simulation is promising method to predict numerous properties of nonaqueous electrolytes, quantitative predictions depend critically on the prescribed force fields. We show that several quantum-mechanically refined force fields for the lithium bis(trifluoromethanesulfonyl)imide (LiTFSI) - acetonitrile electrolyte yield structures agreeing well with the experimental neutron pair distribution function (PDF), yet produce dramatically different dynamics disagreeing with NMR measurements. Such glaring discrepancies indicate that inadequate representation of long-range interactions leads to excessive frustration in the free energy landscape. Better agreement is achieved by proportionally scaling down the atomic charges of the ions. This simplification enabled the simulation of concentration dependences of ionic diffusion for 0.2-2 M LiTFSI solutions without sacrificing fit quality of the PDFs. We argue that not only structures but also dynamics constitute important checkpoints towards to computationally design functional electrolytes.

Acknowledgments

This project would not have been possible without the support of many people. Many thanks to my adviser, Professor Yang Zhang, who read my numerous revisions and gave many useful suggestions. Thanks to many collaborators, Lily A. Robertson, Eli Shkrob, Lu Zhang, and Prof. Jeffery S. Moore, who provide experimental supports, interpretations of experimental data, and numerous revisions of the paper related to this project. Also thanks to my second thesis reader, Prof. Tomasz Kozlowski, who offered guidance and supports. Thanks to my labmates, Zhikun Cai, and Nathan Walter, providing me with generous help to complete this project. And finally, thanks to my husband, parents, and numerous friends, who always offer support and love.

The research was financially supported by the Joint Center for Energy Storage Research (JCESR), an Energy Innovation Hub funded by the U.S. Department of Energy, Office of Science, Basic Energy Sciences. The neutron scattering work is supported by the U.S. Department of Energy, Office of Science, Office of Basic Energy Sciences, Materials Sciences and Engineering Division, under Award Number DE-SC0014084. A portion of this research used the NOMAD instrument at the Spallation Neutron Source, a DOE Office of Science User Facility operated by the Oak Ridge National Laboratory. Access to HFBS was provided by the Center for High Resolution Neutron Scattering, a partnership between the National Institute of Standards and Technology and the National Science Foundation under Agreement No. DMR-1508249. Identification of a commercial product does not imply recommendation or endorsement by the NIST, nor does it imply that the product is necessarily the best for the stated purpose.

Table of Contents

List of Tables

List of Figures

List of Abbreviations

MD	Molecular dynamics.
LiTFSI	Lithium bis(trifluoromethanesulfonyl)imide.
PDF	Pair distribution function.
RFBs	Redox flow batteries.
NRFBs	Nonaqueous redox flow batteries.
DMB	1,4-dimethoxybenzene.
BzNSN	2,1,3-benzothiadiazole.
DBMMB	2,5-di-tert-butyl-1- methoxy-4-[2-methoxyethoxy]benzene.
QENS	Quasielastic neutron scattering.

Chapter 1

Introduction

1.1 Nonaqueous Electrolytes

As the charge-transport medium, electrolytes are ubiquitous in all electrochemical devices such as supercapacitors, solar cells and batteries [1, 2]. An example of Li-ion battery is schematically depicted in Figure 1.1 (derived from [3]). The majority of the electrolytes are electrolyte solutes consisting of salts dissolved in solvent and are in a liquid state at the service-temperature. Ideally, the electrolyte should not to undergo chemical changes during the operation of the device. From an oversimplified view, the electrolytes could be considered as the inert component in the electrical devices, which means that it must encompass good stability. While the potential of the battery are usually quantified by the redox potential in volts, the stability of an electrolyte can be quantified by the range in volts between its oxidative and reductive decomposition limits, which is know as the "electrochemical window". The redox potential must fall within this electrochemical window to enable a rechargeable battery operation.

Regarding the solvent types, either water or organic molecules, electrolytes can be classified to be aqueous and nonaqueous. Nonaqueous solvents show a better electrochemical stability and a wider potential window than aqueous solvents such as water. This can lead to batteries with higher energy densities because redox couples with an elevated voltage can be used. In addition, low vapor pressure, high thermal stability, good dissolution properties, wide liquid-phase ranges, and high electrochemical potential, have made lithium-salt-doped nonaqueous electrolytes the most promising charge-transport media [4, 5].

Electrochemical stability is only one of the requirements that electrolytes should meet. General list of requirements include: good ionic conductivity, wide electrochemical window, inert to other components, and robust against various abuses. In accordance with the basic requirements for electrolytes, an ideal electrolyte solvent should meet the following minimal criteria: ability of dissolving salts to sufficient concentration, low viscosity, and inert to all the other components. Considering these requirements, the nonaqueous compounds that qualify as electrolyte solvents must be able to dissolve sufficient amounts of salt. Only those with polar groups such as carbonyl (C=O), nitrile (C≡N), sulfonyl (S=O), and ether-linkage (O) merit consideration.

An ideal electrolyte solute for ambient rechargeable electrical devices should satisfy these requirements: high solubility and mobility in the media, stability against oxidative decomposition, invert to electrolyte solvents and other components such as separator and substrate. For lithium-ion battery, the available choice of lithium salts for electrolyte application is rather limited when considering nonaqueous solvents. Most of the lithium salts that satisfy the minimum solubility standard are based on complex anions such as hexafluorophosphate (PF_6), perchlorate (ClO_4), bis(trifluoromethylsulfonyl)imid (TFSI).

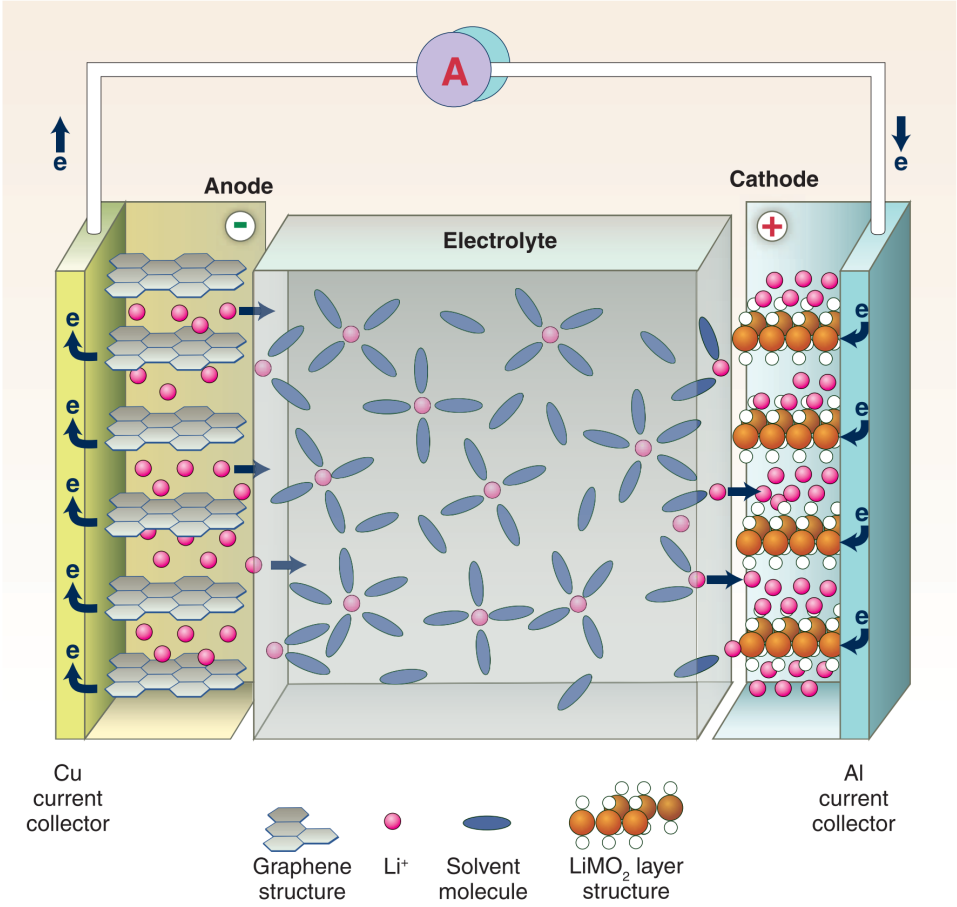

Figure 1.1: Schematic of a rechargeable lithium battery. The anode is a graphitic carbon, whereas the cathode is an oxide. The electrolyte electrodes are separated by a nonaqueous electrolyte that transfers Li ions between the electrodes. (Adapted from Ref. 3)

Although the electrochemical stability of the electrolyte is of significant importance to the rechargeable system, it is often challenged by the strong oxidizing and reducing nature of active materials in the system such as cathode and anode in a battery. This challenge becomes more serious with the increasing of energy density in new batteries since they require a more oxidizing cathode and reducing anode. In addition,

electrolytes in batteries must cater to the needs of both electrodes; hence, new battery chemistries have incurred new electrolyte compositions. Significant attention has been paid to new applications requiring optimized electrolytes such as next generation batteries [1, 2]. Among next generation batteries, nonaqueous redox flow battery is one of the most promising candidates[6, 7] and is also the focus of this project. Thus, we introduce redox flow battery in the following section.

1.2 Redox Flow Batteries

Natural energy sources, such as wind and solar energy, are plentiful, but their intermittency complicates their integration into the electrical grid. Redox flow batteries (RFBs) have the potential to match the supply and demand in time and to make these energy sources competitive with more traditional power sources. A schematic representation taken from Wang et al. [8] is presented in Figure 1.2, which is a type of rechargeable device capable of providing reversible conversion between electrical and chemical energy.

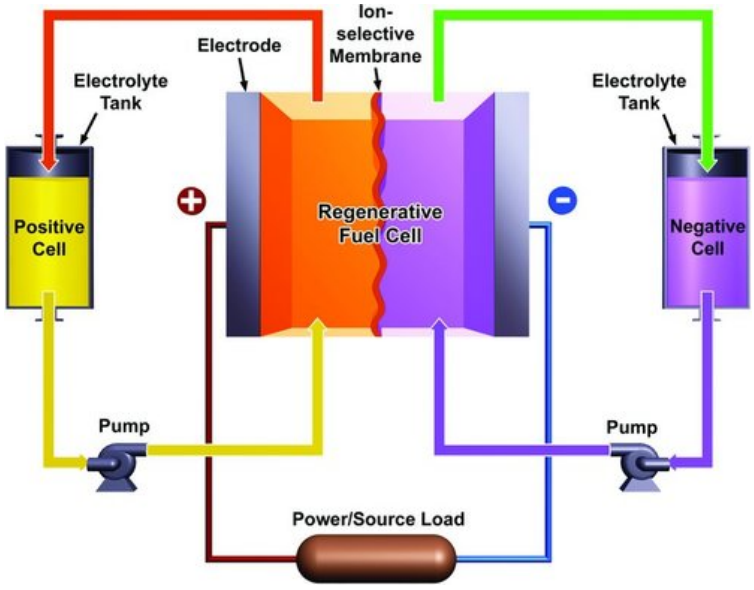

Figure 1.2: Schematic representation of redox flow battery. (Adapted from Ref. 8)

The main components of the redox flow battery are the electrochemical cell and two electrolyte tanks. There are two electrodes and a separator (ion-selective membrane) in the regenerative fuel cell. Pumps are used to drive electrolyte solution to circulate between these components. The redox-active cathode and anode materials are dissolved in the electrolyte, which is called as catholyte and anolyte, respectively. The separator is permeable to the supporting electrolyte (a conducting salt), but impermeable to the redox-active material. This setup enables the power and capacity of the battery to be scaled independently from

each other. The energy conversion between electrical energy and chemical potential occurs instantly at the electrodes once the liquid electrolytes are flowing through the cell. The energy is stored in external electrolyte tanks with flexible size in accordance with the requirements of specific system, while the traditional battery often store energy in the fixed electrode materials, which makes a significant difference in energy capacity. Furthermore, RFBs could be free of a lot of issues due to its unique working mechanism. Firstly, the role of electrode is simplified, only providing active surface for the redox reaction to take place, which hinders the physical and chemical changes on the electrodes according to Wang et al. [8]. And since the working environment is liquid and the reaction material is placed separately, RFBs are safer when compared to conventional batteries. In addition, the configuration of RFBs is simpler and cheaper due to the simplified structure. With these special advantages, the RFBs becomes a leading approach for the stationary energy storage [6]. Li et al. [9] also summarize some advantages of RFBs, which include high energy efficiency, short response time, low self-discharge, long life-time, and independent tunable power and storage capacity.

Currently, there are many types of redox flow batteries including aqueous-based, nonaqueous-based, metal-based, organic-based, and organic-metal combined according to Winsberg et al. [6]. Nonaqueous redox flow batteries (NRFBs) are particularly promising in this regard due to the increased electrochemical stability windows of organic electrolytes compared to aqueous electrolytes [10, 11]. However, to make NRFBs economically competitive, many requirements need to be met. These requirements include active material, salt, and solvent costs, electrochemical stability, solubility, energy density, and area specific resistance [12]. Cost-analysis of NRFBs sets stringent goals for all of these parameters [13]. To reach these goals, better fundamental understanding of the complex interactions in RFBs electrolytes in all states of charge is needed to quantify their limitations and to engineer new electrolytes.

In the flow cells, charge exchange and charge storage are spatially separated (Figure 1.3), which makes these batteries supremely scalable. The stored capacity not only depends on the storage tank volume but also on the concentration and energy density of catholyte (oxidized species) and anolyte (reduced species) in the charged fluid. Organic molecules have great potential as redox active materials in the NRFBs as they can be tailored to meet many of the required properties [14, 15]. 1,4-Dialkoxybenzene (e.g., 1,4-dimethoxybenzene, DMB) and 2,1,3-benzothiadiazole (BzNSN) derivatives are two popular catholyte and anolyte families for NRFBs, respectively. A catholyte molecule stores positive charge when oxidized to become a stable radical cation, whereas an anolyte molecule stores negative charge by becoming reduced to a stable radical anion. The DMB and BzNSN families have been chosen both for their high (low) redox potentials, respectively, and the outstanding stability of their radical ions in liquid electrolytes. A DMB derivative, 2,5-di-tert-butyl-1-methoxy-4-[2-methoxyethoxy]benzene (DBMMB), is a recently established catholyte for NRFBs and

hybrid NRFBs [16, 17, 18], while BzNSN anolyte is known for its low redox potential, high solubility, and low molecular weight. Recent BzNSN−DBMMB prototypes exhibited stable and efficient cycling at concentrations up to 0.5 M [19, 20].

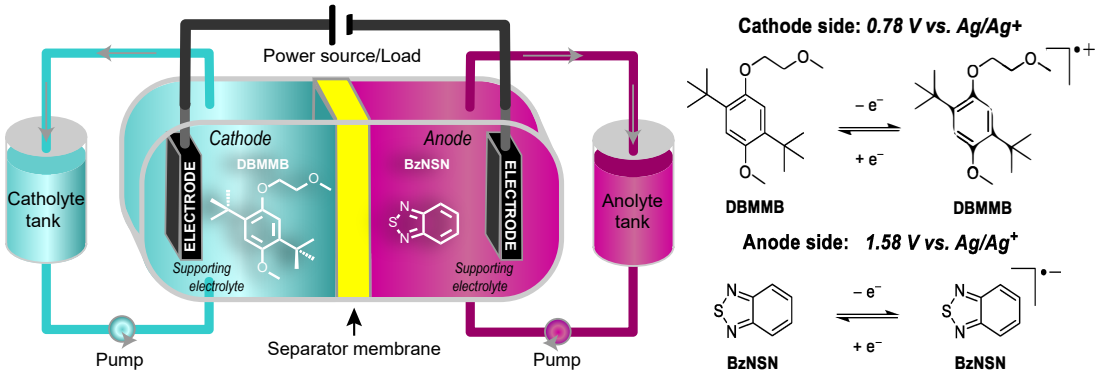

Figure 1.3: General RFB design and family of catholyte (DBMMB) and anolyte (BzNSN) electrolytes studied and corresponding redox potentials in CH_3CN vs. Ag/Ag+ (0.1 M electrolyte, 1 M LiTFSI). (Adpted from Ref. 19)

To obtain energy density targets dictated by the costs analyses, still higher concentrations (1-5 M) of redox-active molecules (ROMs) are required, while most of todays organic electrolytes cannot operate at concentrations $>$ 0.1 M [5]. While the DBMMBBzNSN system performed well below 0.5 M, cycling at 1 M was poor and characterized by increased viscosity and reversal of cell polarization [19]. As such complications are common, it is important to understand which properties of concentrated, multicomponent electrolytes lead to the transport limitations impeding their success in the NRFBs. Here, neutron scattering is used to probe the nanosecond-scale dynamics of complex electrolytes at different temperatures. In the following chapter, a general introduction for neutron scattering technique is provided.

Chapter 2

Materials and Methods

2.1 Experimental Measurements

2.1.1 Neutron Scattering

The structures and dynamics of nonaqueous electrolytes have been studied by many experimental techniques including NMR, X-ray and neutron diffraction, and Raman spectroscopy[21, 22, 23, 24]. Neutron scattering is a powerful technique to probe structures over a length-scale ranging from $\mathring{A}$ to nanometer and dynamics of materials at atomic scale over a timescale ranging from sub-picosecond to tens of nanoseconds owing to comparable wavelength with interatomic spacings and kinetic energy with the atoms. Figure 2.1 shows a schematic geometry set up of neutron scattering experiment. Incident neutrons interact with matter and get scattered with energy and moment exchange. The physical information of the matter can be deduced by measuring the distribution of scattered neutrons as a function of energy and momentum transfer. The interaction strength is proportional to the number of neutrons scattered into a certain solid angle and can be described by double differential cross-section $\frac{d^2\sigma}{d\Omega dE}$ or differential cross-section $\frac{d\sigma}{d\Omega}$. In fact, the direct measurable quantity of neutron scattering is the double differential cross-section or differential cross-section, which contains the coherent and incoherent contribution:

$$\frac{d^2\sigma}{d\Omega dE} = \frac{\sigma_{coh}}{4\pi}\frac{k_f}{k_i}NS(\mathbf{k},w) + \frac{\sigma_{inc}}{4\pi}\frac{k_f}{k_i}NS_s(\mathbf{k},w) \tag{2.1}$$

where $d\Omega$ is the solid angle of scattering, dE is the energy exchange, N is the total atom numbers in the matter, k_i and k_f are the wavevectors of the incident neutron and the scattered neutron, σ is the microscopic cross-section related to element intrinsic characteristics, $\mathbf{k} = \mathbf{k}_f - \mathbf{k}_i$ is the change of wavevectors, w represents the energy exchange, and $S(\mathbf{k},w)$, $S_s(\mathbf{k},w)$ are the coherent and incoherent dynamic structure factor respretively. The physical meaning of dynamic structure factor is easier to interpret in time domain by Fourier transform. The coherent and incoherent dynamic structure factor is the Fourier transform of the coherent and incoherent intermediate scattering function [25]):

$$
\begin{aligned}
S(\mathbf{k}, w) &= \frac{1}{2\pi\hbar} \int F(\mathbf{k}, t) \exp(-iwt) dt \\
S_s(\mathbf{k}, w) &= \frac{1}{2\pi\hbar} \int F_s(\mathbf{k}, t) \exp(-iwt) dt
\end{aligned}
\tag{2.2}
$$

where coherent intermediate and incoherent intermediate function are:

$$
\begin{aligned}
F(\mathbf{k}, t) &= \frac{1}{N} \sum_{j,j'} \langle \exp(-i\mathbf{k} \cdot \mathbf{R}_{j'}(0)) \exp(-i\mathbf{k} \cdot \mathbf{R}_j(t)) \rangle \\
F_s(\mathbf{k}, t) &= \frac{1}{N} \sum_{j} \langle \exp(-i\mathbf{k} \cdot \mathbf{R}_j(0)) \exp(-i\mathbf{k} \cdot \mathbf{R}_j(t)) \rangle
\end{aligned}
\tag{2.3}
$$

where $\mathbf{R}_j(t)$ is the j_{th} particle position in the matter at time t, and $\langle\rangle$ is the ensemble average. Notice that:

$$
\begin{aligned}
\exp(-i\mathbf{k} \cdot \mathbf{R}(t)) &= \int \delta\{\mathbf{R} - \mathbf{R}(t)\} d\mathbf{R} \\
\rho(\mathbf{R}, t) &= \sum_j \delta\{\mathbf{R} - \mathbf{R}(t)\} \\
\rho(\mathbf{R}, t) &= \sum_j \delta\{\mathbf{R} - \mathbf{R}(t)\} = \rho_{\mathbf{k}}(t)
\end{aligned}
\tag{2.4}
$$

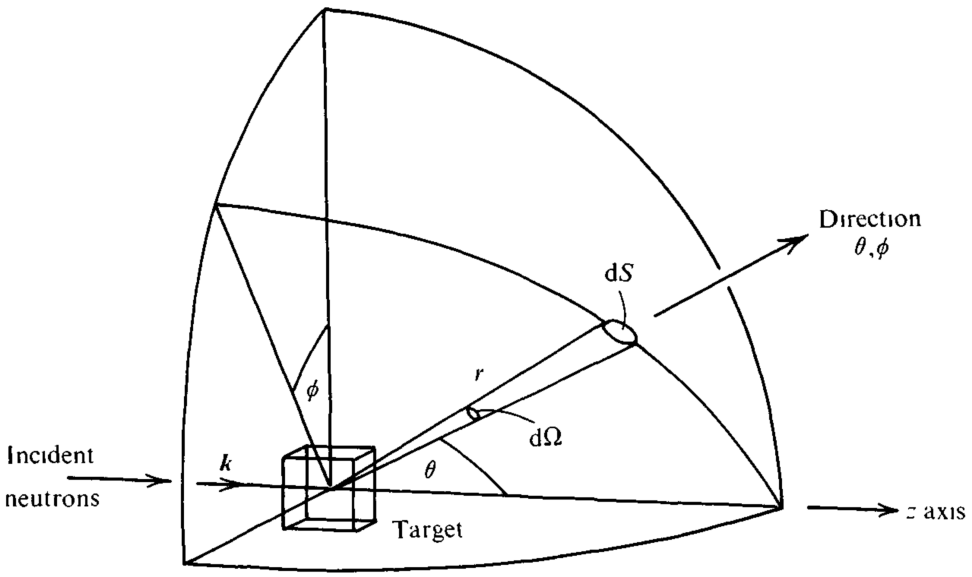

Figure 2.1: Geometry for neutron scattering experiment. (Adapted from Ref. 25)

where $\rho_{\mathbf{k}}(t)$ is the Fourier transform of atom number density. Then $F(\mathbf{k}, t)$ could be written as:

$$
F(\mathbf{k}, t) = \frac{1}{N} \langle \rho_{\mathbf{k}}(0) \rho_{\mathbf{k}}(t) \rangle \tag{2.5}
$$

From equation 2.5, $F(\mathbf{k}, t)$ is time dependent density correlations. It depends on the correlation between the same atom at different times, and on the correlation between different atoms at different times, which gives interference effects and describes the collective motions in materials. While $F_s(\mathbf{k}, t)$ only relies on the correlation between the positions of the same atom at different times. Therefore, incoherent scattering is related with self motions.

As shown in equation 2.1, cross section, $\sigma_{coh}, \sigma_{inc}$, determines the strengths of coherent and incoherent contributions. Thus neutron scattering is very sensitive to materials element composition. The incoherent cross section of hydrogen (∼80 b) is much larger than its coherent cross section (∼1.8 b) and other elements (∼5 b for deuterium, carbon, oxygen). Therefore, for a hydrogen-rich system, neutron scattering mainly measures the self dynamics, which is the technique we use to probe the dynamics of our nonaqueous electrolyte. To get the dynamical information of a specific component, we need to hide the contributions from other components. Deuteriation is a common used method as the cross section of deuterium is much smaller than hydrogen. In this study, selectively deuterated ROMs allow highlighting the chemical species of interest (Figure 2.2). DMB is used as a model catholyte ROM in our study since deuterated DBMMB is cost-prohibitive to synthesize. Thus, DMB-d10 was obtained by methylation of hydroquinone with methyliodide-d3 followed by proton exchange using trifluoroacetic anhydride (TFAA) in D_2O. BzNSN was synthesized in a reaction of 1,2-diaminobenzene with $SOCl_2$ [26]. BzNSN-d_4 was synthesized using the same method after platinum/carbon HD exchange of 1,2-diaminobenzene in D_2O [27]. DBMMB was synthesized according to literature procedure [17].

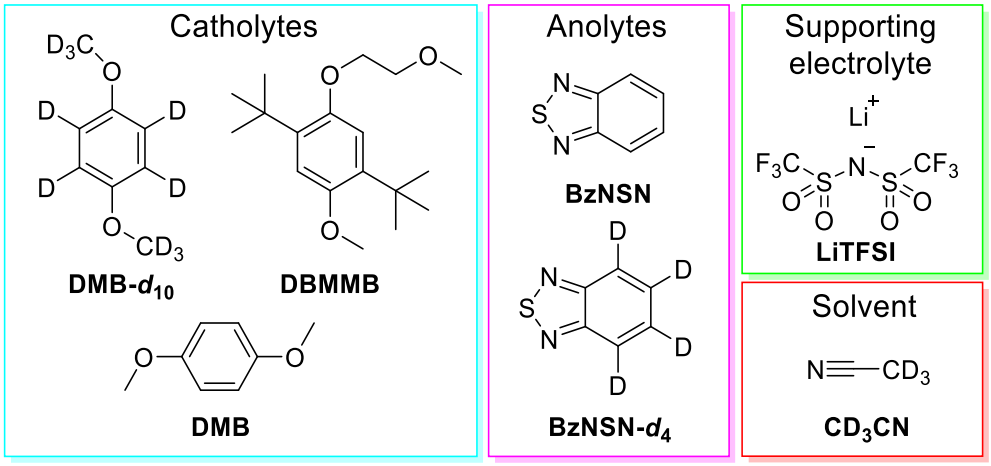

Figure 2.2: Deuterated and protiated ROMs (DBMMB, DMB, BzNSN) and other electrolyte components used in neutron scattering experiment.

In this thesis, the specific neutron scattering technique we used to probe dynamics is quasielastic neutron

scattering (QENS). A schematic representation of QENS in energy exchange domain is provided in Figure 2.3. Quasielastic means that the energy exchange is small, usually in μeV magnitude. Therefore, QENS could probe the diffusion process at atomistic scales and time (ps to ns) simultaneously, including rotational and translational motion. Another feature of QENS is that either incoherent or coherent scattering can be dominate by selective deuteration. For hydrogenated system having large incoherent scattering cross section, the self-diffusion process can be examined. On the other hand, collective dynamics information could be obtained for derterated system where coherent scattering is dominant.

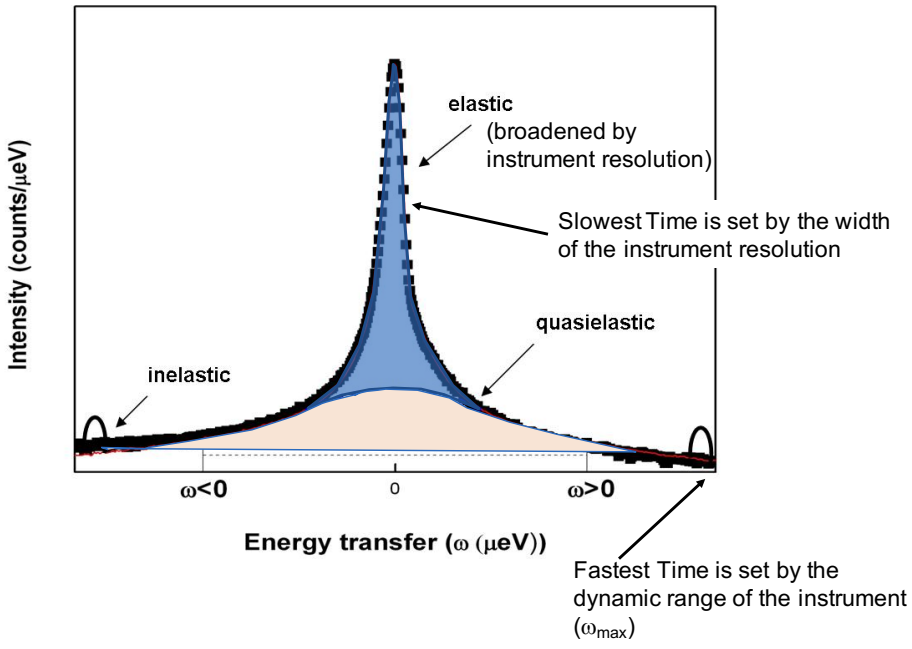

Figure 2.3: Illustration of QENS in energy transfer domain.

2.1.2 Quasi-elastic Neutron Scattering

The QENS measurements were performed at the NIST Center for Neutron Research (NCNR). The high flux backscattering (HFBS) instrument was used in both fixed-window and dynamic-window modes. The incident neutron wavelength was 6.271 Å, which is equivalent to an energy of 2.08 meV. Thin-layer chromatography was performed using on F-254 precoated silica gel plates and visualized using 254 nm light. Chromatography was performed using 60 Å silica gel from Silicycle, Inc. Differential scanning calorimetry (DSC) measurement was performed using a TA Instruments Q20 differential scanning calorimeter. Fixed window scans were acquired between 4 K and 298 K as the temperature first decreased and then increased at a constant rate of 0.9 K/min. In this mode, the instrument records only elastic scattering (with the Doppler drive stopped).

In the dynamic mode (with the Dopper drive on), 1 M DBMMB sample was studied. The Si(111) crystal monochromator was operated at 24 Hz, providing a dynamic range of 17 eV, an energy resolution of 1 eV at the elastic peak and a Q range of 0.25 to 1.75 $Å^{-1}$. Quasi-elastic spectra were obtained at 250 K, once after cooling and once after heating at 0.9 K/min as in the fixed-window scan.

All starting materials were dried using the Schlenk line on ice for 5 min followed by argon backfill three times (DMB and BzNSN easily sublime) and transferred to the glovebox in an argon-sealed vial. Representative sample preparation: An oven-dried 5-mL volumetric flask and 20-mL I-CHEM vial were added to an argon-filled glovebox. DMB (0.345 g, 2.5 mmol), BzNSN-d4 (0.351 g, 2.5 mmol) and LiTFSI (1.434 g, 5.0 mmol) were added to the volumetric flask and dissolved in CD_3CN-d_3 to give a solution containing the electrolytes in 0.5 M, 1.0 M, and 1.5 M concentrations, respectively. The complete list of samples measured at fixed window scan is given in Table 2.1, and only 1.0 M DBMMB was measured at dynamic mode due to time limitation.

Table 2.1: Samples measured for neutron scattering experiment

Sample name	Hydrogenated	Deuterated
0.5 M BzNSN	0.5 M BzNSN	0.5 M $DMBd_{10}$
1.0 M BzNSN	1.0 M BzNSN	1.0 M $DMBd_{10}$
1.5 M BzNSN	1.5 M BzNSN	1.5 M $DMBd_{10}$
0.5 M DMB	0.5 M DMB	0.5 M BzNSN-d_4
1.0 M DMB	1.0 M DMB	1.0 M BzNSN-d_4
1.5 M DMB	1.5 M DMB	1.5M BzNSN-d_4
0.5 M DBMMB	0.5 M DBMMB	0.5 M BzNSN-d_4
1.0 M DBMMB	1.0 M DBMMB	1.0 M BzNSN-d_4
1.5 M DBMMB	1.5 M DBMMB	1.5M BzNSN-d_4
Control	1.0 M LiTFSI	

Liquid samples (3 mL) were transferred to cylindrical HFBS sample cans (1 mm thickness) in a helium-filled glovebox. Helium was used to exclude moisture and enhance heat conductivity. Sample cans were cleaned thoroughly with ethanol prior to preparation. Indium wire was used to effectively seal the can. For a detailed picture of the sample cans, see https://www.ncnr.nist.gov/instruments/hfbs/samp-enviro.html. The sample was removed from the glovebox and attached to the sample stick, which was lowered into the HFBS chamber, and the chamber was evacuated and backfilled with helium three times. The HFBS control setup was set to a fixed window scan (i.e., no Doppler drive), which allows detection of elastically scattered

neutrons only. The fixed window scan was performed at 0.9 K min^{-1} from 4 K to 298 K with an accuracy better than 0.1 K with the cooling scan performed first and the heating scan second.

2.1.3 Neutron PDF Measurements

In addition to dynamical information, neutron scattering could also be used to investigate structural properties. By integrating over energy exchange (w) of equation 2.1, we get:

$$\frac{d\sigma}{d\Omega} = \sigma_{coh} N S(\mathbf{k}) + \text{constant} \tag{2.6}$$

where the constant comes from incoherent scattering due to isotropic contribution and $S(\mathbf{k})$ is called the structure factor:

$$\begin{aligned} S(\mathbf{k}) &= \frac{1}{N} \left\langle \sum_{i,j} \exp(-i\mathbf{k} \cdot (\mathbf{R_i} - \mathbf{R_j}) \right\rangle \\ &= 1 + \int (g(\mathbf{R}) - \tilde{\rho}) \exp(-i\mathbf{k} \cdot \mathbf{R}) \end{aligned} \tag{2.7}$$

where $g(\mathbf{R})$ is known as pair distribution function, which gives the probability that there is an atom, i, at distance R from the origin of a coordinate system, given that there is also a different atom at the origin of the coordinate system at the same instant in time:

$$g(\mathbf{R}) = \sum_{i \neq 0} \langle \delta(\mathbf{R} - \mathbf{R}_i + \mathbf{R}_0) \rangle \tag{2.8}$$

From $g(\mathbf{R})$, the average distance of the nearest neighbors, second nearest neighbors, the coordination number can be directly determined. In this thesis, we performed neutron paid distribution function (NPDF) measurement to get structural information.

Neutron PDF measurements were performed at the nanoscale-ordered materials diffractometer (NOMAD) beamline of the Spallation Neutron Source (SNS) at Oak Ridge National Laboratory (ORNL)[28]. The maximum Q is 25 Å^{-1} and the Lorch function are applied to the data. To reduce incoherent scattering from hydrogen, deuterated acetonitrile was used. The samples were prepared in a Braun argon-filled glovebox and sealed in 1 mm diameter quartz capillaries. 0.5 h acquision time was necessary to obtain a high resolution PDF data at room temperature.

2.1.4 NMR Measurements

To estimate diffusion coefficients for the component ions Li^+ and $TFSI^-$, at room temperature, pulsed-field gradient stimulated spin-echo NMR (PGSE NMR) [29, 30] with longitudinal eddy current delay, bipolar gradients, and convection compensation was used. A DOSY/diffusion module on a Bruker Avance III HD spectrometer operating at 300 MHz was used for data collection and processing. For consistency, LiTFSI was also dissolved in deuterated acetonitrile. Lithium-7 resonance from the Li^+ ions and fluorine-19 resonance from the $TFSI^-$ anions was used to obtain the coefficients for translational diffusion in the gradient of the magnetic field.

2.2 Molecular Dynamics Simulation

Complementary to experiments, molecular dynamics (MD) simulations have been used to predict structural, thermodynamic, and transportation properties of electrolyte solutions. Realization of the power of MD simulations in predicting properties and assisting in interpreting experimental data has attracted tremendous interest [31, 32, 33]. Central to the accurate prediction of computed properties from MD simulation is the prescribed force field. High quality of prescribed force fields are critical to the reliability of such computations.

Currently, there are two kinds of force fields that are used in MD simulations. Non-polarizable force fields include intramolecular contributions of bond stretching, angle bending, and dihedral angle torsional motion, and intermolecular contributions given by the Lennard-Jones and Coulomb interactions, which takes the standard form:

$$\begin{aligned} V_{\text{nonpolarizable}} = &\sum_{\text{bonds}} k_b(r-r_0)^2 + \sum_{\text{angles}} k_\theta(\theta-\theta_0)^2 + \sum_{\text{dihedrals}} V_n[1+\cos(n\phi-\delta)] \\ &+ \sum_i \sum_{j>i} \left\{ 4\epsilon \left[\left(\frac{\sigma}{r_{ij}}\right)^{12} - \left(\frac{\sigma}{r_{ij}}\right)^{6} \right] + \frac{1}{4\pi}\frac{q_i q_j}{r_{ij}} \right\} \end{aligned} \tag{2.9}$$

where r_{ij} is the distance between atom i and j, which carry partial charges q_i and q_j, respectively. Polarizable force fields also include electron polarization of the constituent molecules and ions as additional components.

$$V_{\text{polarizable}} = V_{\text{nonpolarizable}} - \frac{1}{2}\sum_i \mu_i \cdot \mathbf{E}_i^0 \tag{2.10}$$

where $\mu_i = \alpha_i \mathbf{E}_i^{tot}$ is induced dipole of atom i, α_i is the isotropic atomic polarizability, $\mathbf{E}_i^{tot}$ is the total electrostatic filed at atom i due to fixed charges q_i and induced dipoles μ_i, $\mathbf{E}_i^0$ is the electric field contributed by fixed charges only.

Among non-polarizable force fields, the Optimized Potentials for Liquid Simulations-All Atom (OPLS-AA) [34] force field is one of the most widely used [24, 35]. However, the parameterization of this force field has been benchmarked only against select thermodynamic and structural properties [34] with little or no consideration for dynamic properties. Several studies have shown that non-polarizable force fields tend to yield unrealistically slow dynamics [36, 37, 38]. This situation is partially remedied using polarizable force fields. Many well-tested polarizable force fields exist for aqueous systems, however, the development and testing of such force fields for nonaqueous systems lags far behind. A polarizable force field, Atomistic Polarizable Potential for Liquids, Electrolytes, and Polymers (APPLE&P), was developed by Borodin et al. [31] who reported better agreement of predicted dynamic properties (including ion diffusivity, relaxation time, and electrical conductivity) with experiments [39]. Despite these advances, there are still significant discrepancies between the dynamic predictions of MD models and experiments.

Here, we show that a simple modification of the non-polarizable force field can simultaneously achieve robust representation of electrolyte structure and ionic diffusivity in a nonaqueous electrolyte. To this end, several non-polarizable force fields were constructed, and MD simulations using these force fields were compared with the neutron pair distribution function (NPDF) and ion diffusivity measurements for acetonitrile (CH_3CN) containing 0.2 to 2 M lithium bis(trifluoromethanesulfonyl)imide (LiTFSI). Due to its relative simplicity and practical significance, this electrolyte/solvent pair has become the supporting electrolyte in the redox flow battery and test bed for addressing challenges in nonaqueous force field development [22, 32, 40, 19].

2.2.1 Force Field Development: Quantum Chemistry Calculations

Molecular Dynamic simulations were performed based on OPLS-AA force field. Firstly, quantum chemistry calculations were performed to optimize the partial charge and geometry since it is also known that the OPLS-AA force field is aiming at a transferable model to simulate any liquid by building the molecular structure with corresponding atom types without considering the specific molecular structure and interaction. The quantum chemistry methods we chose here contain Mller-Plesset second order perturbation theory (MP2) with aug-cc-pVDZ basis set and B3LYP with 6-31/G(d) basis set. These two methods and basis set are chosen according to a pioneering work by Martin [41], which reported these two methods gave more accurate predictions on the partial charge. The calculation were performed on both clusters and isolated molecules by using Gaussian09 package [42]. Charges from electrostatic potentials using a grid based method (CHelpG) [43] method is used to extract the partial charges. Atoms belonging to the same type have partial charge constrained to the average charge of this type. The basis set superposition error (BSSE) is only considered

for clusters since some literature reported BSSE correction is negligible for isolated molecules [44]. The difference between isolated ions and ions in cluster is not obvious, so we use the partial charge computed by isolated ions in this work. Figure 2.4 is the electrostatic potential surface for $TFSI^-$ anions. The potential surface is almost identical for these two methods, but the partial charge is slightly different after implementing CHelpG method.

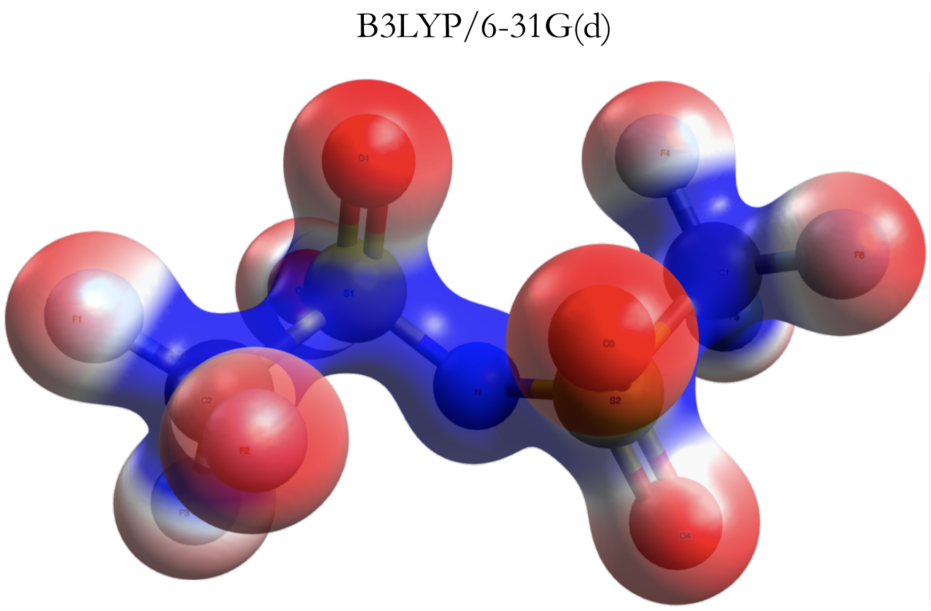

Figure 2.4: Electron deinsity surface of TFSI with electrostatic potential color map for B3LYP/6-31G(d).

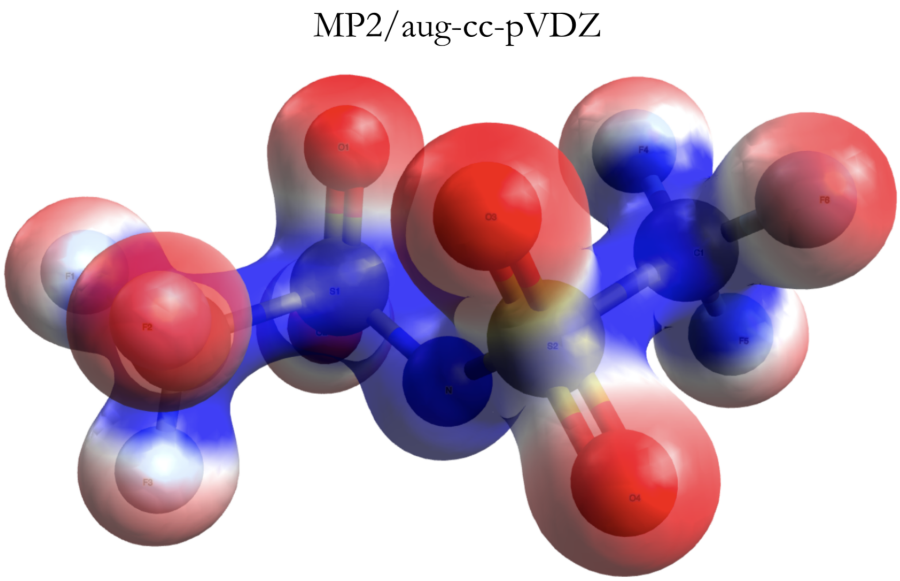

Figure 2.5: Electron deinsity surface of TFSI with electrostatic potential color map for MP2/aug-cc-pVDZ.

Table 2.2: Comparison of the partial atomic charge extracted by CHelpG for $TFSI^-$ among MP2, B3LYP, original OPLS-AA.

Atom type	B3LYP	MP2	OPLS-AA
C	0.353	0.553	-0.184
N	-0.645	-0.676	-0.146
O	-0.505	-0.59	-0.646
F	-0.137	-0.21	-0.015
S	0.891	1.095	1.094

Table 2.3: Comparison of the partial atomic charge extracted by CHelpG for Acetonitrile among MP2, B3LYP, original OPLS-AA

Atom type	B3LYP	MP2	OPLS-AA
C1	-0.256	-0.122	-0.08
C2	0.375	0.352	0.46
N1	-0.461	-0.494	-0.56
H1	0.114	0.088	0.66

2.2.2 MD Simulation Procedures

The MD simulations were performed with the Gromacs(5.1.4) package[45, 46, 47, 48]. There are 1000 MeCN and 100 LiTFSI for 1.5 M in a cubic box, where periodic boundary conditions are enforced in three dimensions. The density ρ of the electrolyte was estimated from a quadratic fit to experimental values and fixed during MD simulation.

$$\rho(g/cm^3) = 0.8779 + 0.1758c - 0.0044c^2 \tag{2.11}$$

where c is the molarity of LiTFSI. The configuraton of the simulation box at 0.2 M to 2 M is shown in Table 2.4.

Table 2.4: Simulation box configuration at different concentration

Concentration (M)	Density (g/cm^3)	# Solvent	# Salt	Simulation box length (nm)
0.2	0.8789	4500	50	7.378
0.3	0.8963	3000	50	6.475
0.4	0.9136	2250	50	5.908
0.5	0.9308	3600	100	6.939
1.0	1.0154	1600	100	5.454
1.5	1.0978	1000	100	4.792
2.0	1.1780	1200	200	5.377

Initial configurations were obtained with the Packmol package [49]. Further energy minimization is applied to remove the unreasonable contacts resulting from the initial random configuration in the system using the steepest decent method. The maximum step size and the tolerance are set to 0.01 nm and 10 kJ nm^{-1} mol^{-1}. Particle-Mesh Ewald (PME) method was used to deal with long-range Coulomb interactions. For the Lennard-Jones interactions, the cut-off distance and neighbor searching distance are 1 nm. Further, the configuration went through a equilibrating process of 4 ns at 300 K in NVT ensemble using the V-rescale thermostat with a coupling constant of 1 fs. Production runs were 10.0 ns long. The relevant quantities are calculated by averaging over a large subset of the trajectories.

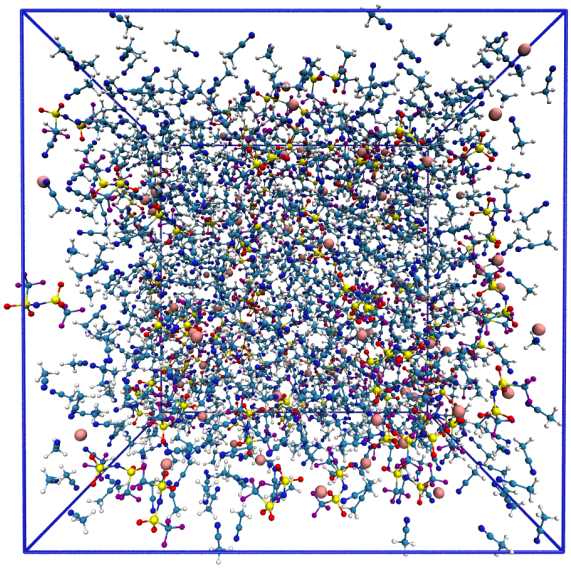

Figure 2.6: Snapshot of simulation box (1.5 M LiTFSI dissolved in C_3CN). Li^+ (pink), H (white), O (red), S (yellow), C (light blue), N (heavy blue).

2.2.3 Protocols for Calculating PDF, Structure Factor, and MSD from MD Simulation

To compare MD simulation predictions with NPDF and NMR, we calculated related quantities using the package developed in our group [50]. The following are the computational details.

In isotropic medium, the radial PDF $g(r)$ depends only on the relative interatomic distance $r = |r|$. To compare with NPDF measurement, here we consider the scattering length and can be computed from MD simulation as follows:

$$g(r) = \frac{1}{4\pi r^2 dr \rho N \langle b \rangle^2} \left\langle \sum_{l \neq l'} b_l b_{l'} \delta(\mathbf{r} - |\mathbf{r}_l - \mathbf{r}_{l'}|) \right\rangle \tag{2.12}$$

where b_l is the coherent neutron scattering length for nucleus l, $\mathbf{r}_l$ is the radius vector to this nucleus, $\mathbf{r}$ is the radius vector between a pair of nuclei, $\langle b \rangle$ is the mean coherent neutron scattering length, ρ is the average number density, and the brackets in this equation mean averaging over the macroscopic ensemble of N nuclei. The structure factor $S(k)$ depends on the modulus k of the scattering vector $\mathbf{k}$ as:

$$S(k) = \frac{1}{N \langle b \rangle^2} \left\langle \sum_{l \neq l'}^{N} b_l b_{l'} \exp\{-i\mathbf{k} \cdot [\mathbf{r}_l - \mathbf{r}_{l'}]\} \right\rangle \tag{2.13}$$

The mean squared displacement $\langle r^2(t) \rangle$ (MSD) for ions is defined as:

$$\langle r^2(t) \rangle = \frac{1}{N} \left\langle \sum_{l=1}^{N} (\mathbf{r}_l(t) - \mathbf{r}_l(0))^2 \right\rangle \tag{2.14}$$

where the summation is taken over all atoms in a given ion, and the averaging is taken over all like ions in the ensemble at two points in time. The diffusion coefficient is estimated from the slope of MSD vs. time according to:

$$\lim_{t \to \infty} r^2(t) = 6Dt \tag{2.15}$$

Chapter 3

Neutron Scattering Measurements of Two Nonaqueous Electrolyte Solutions

Herein, we probe the dynamics of complex ROM fluids containing a catholyte (oxidized species) and an anolyte (reduced species) and supporting electrolyte, LiTFSI, as an indirect but sensitive indicator of the molecular structure. Specifically, we examined two model systems based on DMB and DBMMB. Due to the large incoherent neutron scattering cross-section of H^1 relative to H^2 and other atoms in the sample, only one ROM component was protonated while other components were deuterated to mask their presence. In this way, neutron scattering can probe phase transition and self-diffusion at molecular level.

3.1 Elastic Neutron Scattering

The elastic scattering is dominated by the incoherent scattering for protiated ROMs, and the scattering intensity is proportional to the effective Debye-Waller factor. The normalized elastic incoherent scattering intensity can be described as a function of Q^2 ($Q = |\mathbf{k}|$) [51, 16, 52]:

$$\tilde{I}_T(Q, E = 0) = \frac{I_T(Q, E = 0)}{I_{T_0}(Q, E = 0)} = \exp\left[(-\langle x^2(t)\rangle Q^2 + \frac{1}{2}\alpha_2(t)\langle x^2(t)\rangle^2 Q^4 + ...\right] \tag{3.1}$$

where $\langle x^2(t)\rangle = \frac{\langle r^2(t)\rangle}{6}$ is the mean squared displacement (MSD) and $\langle \alpha_2(t)\rangle = \frac{3\langle x^4(t)\rangle}{5\langle x^2(t)\rangle^2} - 1$ is a dimensionless non-Gaussian parameter, which provides a major adjustment to the Gaussian estimation of the self-intermediate scattering function [16]. The scattering intensity $I_{(T_0)}$ at the base temperature $T_0 = 0$ K was approximated by the value obtained at 4 K when almost all the relaxation degrees of freedom are frozen. Since the instrument has a finite energy resolution, the measured intensity is averaged over the instrument resolution window, which is roughly a few nanoseconds given the 1 μeV energy resolution. Therefore, the MSD is also averaged over the instrument resolution window, containing the summation of all degrees of freedom (translational, rotational, vibrational, etc.).

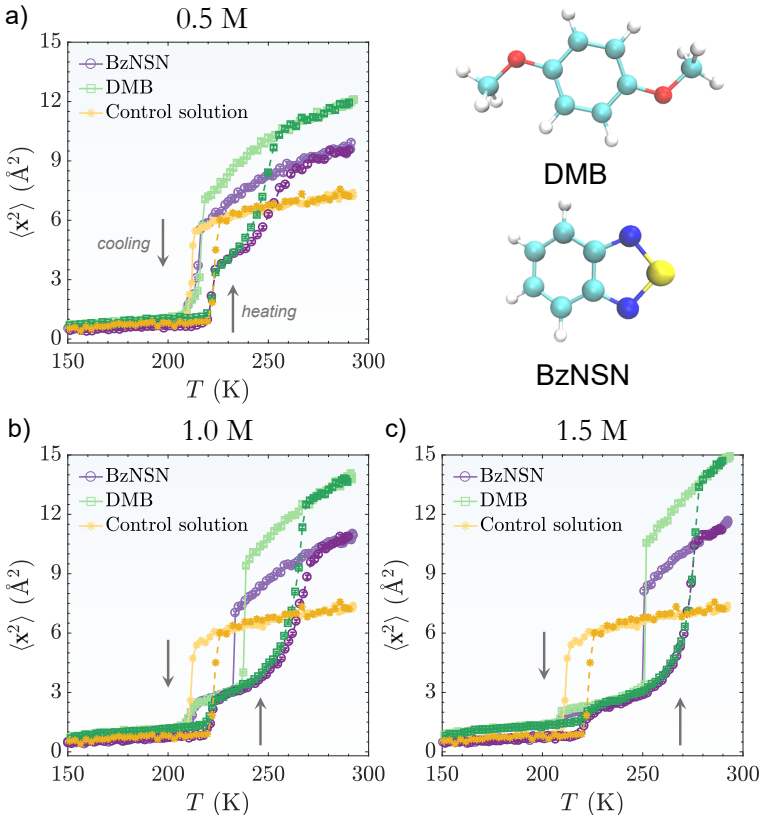

Figure 3.1: Expanded elastic fixed window scans fitted to the mean square displacement (MSD) of the BzNSN (purple circles) and DMB (green squares) at 0.5, 1 and 1.5 M (panels a to c). All samples contain 1 M LiTFSI in CD_3CN. The curve from the control solution is given by the yellow asterisks in all three graphs. Cooling or heating direction is indicated by the arrow, and the heating curve is emphasized by a darker shade.

Figure 3.1 shows the extracted MSD at different temperatures during the scan. The control electrolyte containing no ROMs exhibits abrupt changes of ∼6 Å^2 on cooling and heating with a hysteresis of 15 K. These features are attributed to CD_3CN crystallization, as suggested by differential scanning calorimetry measurements (shown in Figure 3.2). The observed hysteresis may due to strong association of the solvent with Li^+ ions, which causes the freezing point depression in addition to normal supercooling [22] (as suggested by other studies on LiTFSI/CH_3CN solutions). The solutions of BzNSN (with masked DMB-d_{10}, purple circles) or DMB (with masked BzNSN-d_4, green squares) also exhibit an abrupt change that at 0.5 M coincides in temperature with CD_3CN crystallization (Figure 3.1a) but changes at 1 M and 1.5 M (Figure 3.1b and 3.1c, respectively), so that there is a separation ∼40 K between the two transitions at 1.5 M ROM. At this concentration, the crystallization of ROMs from solution occurs around 250 K, and the corresponding

melting events of DMB and BzNSN on warming have hysteresis of *sim*25 K each. Furthermore, the melting events, especially at high concentrations, were found to span a wide temperature.

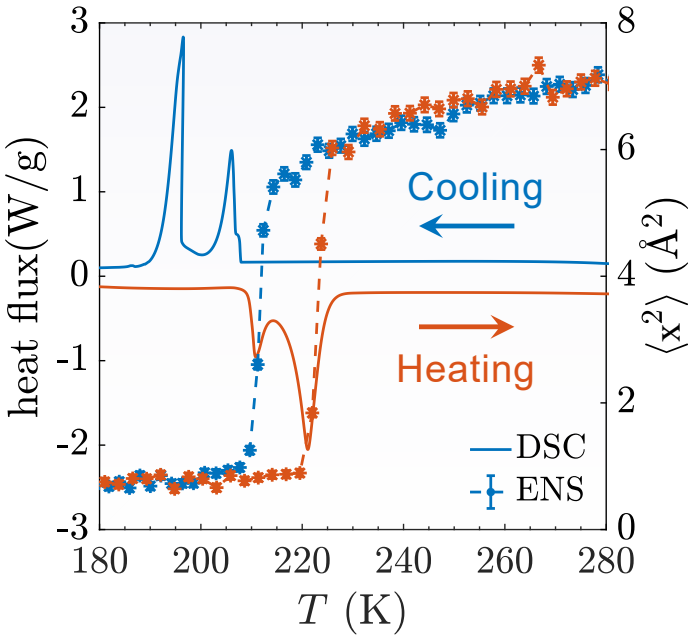

Figure 3.2: Overlaid DSC trace and elastic neutron scattering (ENS) spectra for 1.0 M LiTFSI. The large DSC exotherm on heating correlates with the observed transition in the fixed window scan and corresponds with melting of acetonitrile at 228 K.

The tendency of these aromatic molecules to crystallize is expected from their tendency to form $\pi - \pi$ stacks. DMB and BzNSN also easily sublimate. Even sitting in a vial over minutes at room temperature on the lab bench, crystallites can be observed forming at the top of the vial over minutes. Simple DMB homologs are known to form macroscopic crystals in which the molecules arrange in parallel planes with the arene rings alternating between these planes. The oxygen atoms in the DMBs stabilize one of the benzene resonance forms based on a deformation of the benzenoid ring. BzNSN derivatives also readily form crystals in which these molecules are arranged by $\pi - \pi$ stacking and through intermolecular coordination of their N and S atoms [53, 54]. These relatively strong interactions reduce the entropic costs associated with crystallization [55].

In contrast to DMB, by design DBMMB has structural features intended to reduce its ability to crystallize, so neat compound is liquid at 295 K. Specifically, this catholyte ROM has two bulky tert-butyl groups that prevent $\pi - \pi$ stacking and a methoxyethoxy group that gives this molecule nonzero dipole moment and

depresses the melting point. The unsubstituted oxidized DMB is chemically unstable, as the radical cation rapidly attacks the parent molecule by addition to the arene ring [56]. To preclude this reaction, the arene ring is protected using the tert-butyl groups, which reduce molecular solubility and increase hydrophobicity [57, 58]. Introduction of the methoxyethoxy group improves this solubility and the coordination of Li^+ ions in the electrolyte [17].

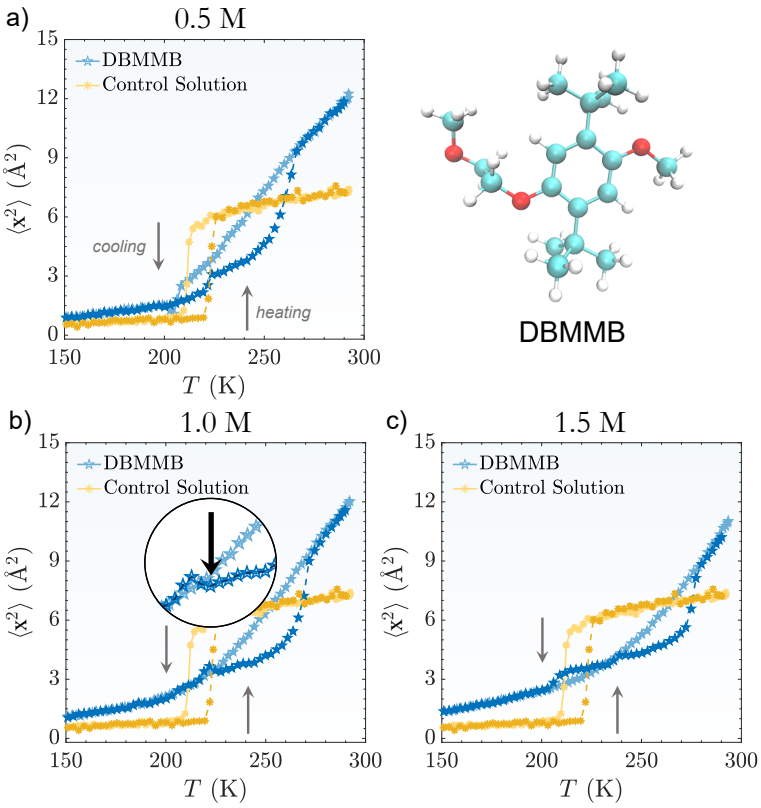

Figure 3.3: Expanded elastic fixed window scans fitted to the MSD DBMMB (blue circles) electrolytes containing 0.5 M, 1 M, and 1.5 M ROMs in CD_3CN. The inset in panel b represents the cold crystallization event. The control curve is represented yellow asterisks in all graphs. Cooling or heating direction is indicated by the arrow, and the heating curve is emphasized by a darker shade.

Figure 3.3 shows the expanded MSD plots for DBMMB (with masked BzNSN-d_4) as a function of the sample temperature. These data are markedly different from the results shown in Figure 3.1. The 0.5 M DBMMB solution (Figure 3.3a) showed only small MSD transitions overlapping with the CD_3CN crystallization of the control solution. At higher concentrations, the electrolytes and solvent did not crystallize at all, instead forming supercooled solutions (Figure 3.3b and 3.3c, cooling curves); only little melting was observed on subsequent heating of these solutions. Additionally, there is evidence for a cold crystallization,

as indicated by a slight dip in MSD shown in the inset in Figure 3.1b. For the 1.5 M DBMMB electrolyte (Figure 3.3c), multiple small-amplitude melting events are observed on heating that cannot be attributed to a specific component. For all concentrations, phase transitions on heating occur over a broad temperature range. To obtain more insight into these transformations, quasi-elastic neutron scattering (QENS) was used.

3.2 Quasi-Elastic Neutron Scattering (QENS)

The QENS amplitude is the sum of the elastic and quasi-elastic scattering contributions given by the Fourier transform of the self-intermediate scattering function. Thus, the QENS intensity can be fitted by:

$$I_T(Q,E) = N \cdot [f(Q)\delta(E) + (1 - f(Q))\mathcal{F}(F_s(Q,t))] \otimes R(Q,E) \tag{3.2}$$

where N is the normalization factor, $F_s(Q,t)$ is the self-intermediate scattering function, $R(Q,E)$ is the Q-dependent energy resolution function, and $\otimes$ is the convolution operator. While the latter includes the translational and rotational components, the rotational dynamics (∼picoseconds typically) are much faster than translational dynamics (∼nanoseconds typically) at measured temperature (250 K) and thus cannot be observed within the dynamic window of our measurement. Therefore, $F_s(Q,t)$ acquires the simple stretched exponential form given by:

$$F_s(Q,t) = \exp\left(-\left(\frac{t}{\tau(Q,T)}\right)^{\beta(Q,T)}\right) \tag{3.3}$$

where τ is the relaxation time, and $\beta(Q,T)$ is the stretching exponent. For simple liquid, the Q-dependence of the relaxation time could be fitted with the jump diffusion model:

$$\frac{1}{\tau(Q,T)} = \frac{D(T)Q^2}{1 + D(T)Q^2\tau_0} \tag{3.4}$$

where D is the diffusion coefficient and τ_0 is the residence time between random jumps of molecules [59, 60, 61]. The resulting curves are shown in Figure 3.4.

Figure 3.4 shows the fitted QENS spectra at three Q values for 1 M DBMMB. All spectra are at 250 K but are measured either after cooling or heating to 250 K as in the fixed-window scan (i.e., the system is in a supercooled or post-cold crystallization state). In the spectra obtained after cooling to 250 K, the elastic scattering component of the fit is weak. As Q decreases, the line becomes broadened, indicating faster dynamics. Conversely, the spectra obtained at 250 K after heating have narrower peaks and there is little

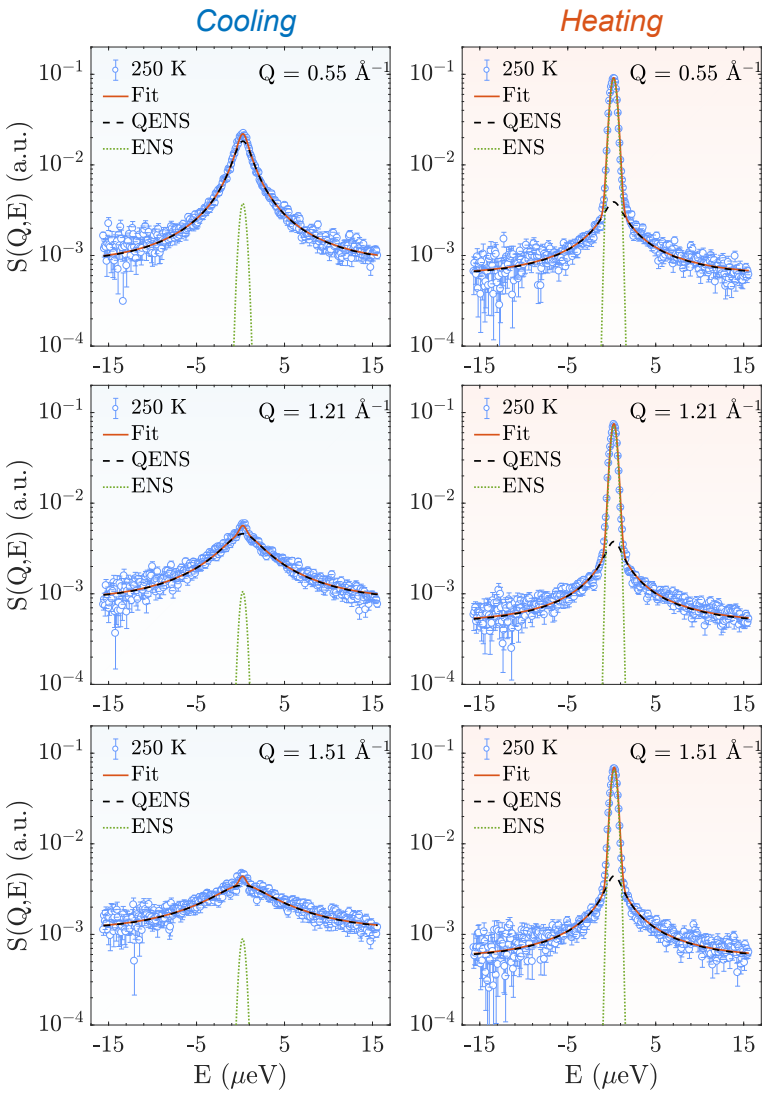

Figure 3.4: QENS spectra of a 1 M DBMMB solution at 250 K. The solution is cycled as in the fixed-window scan with isothermal holds at 250 K for the measurement on cooling or heating. The overall fit (the orange line) is the sum of the elastic (ENS, green dotted line) and inelastic (QENS, dark purple dashed line) contributions. For cooling $\beta = 0.65$, while for heating $\beta = 0.5$.

change with decreasing Q. Here, both elastic and inelastic scattering components are clearly present. These data reveal that the probed molecules move more slowly in the heating curve compared to the cooling curve. In the plots of the relaxation rate ($1/\tau$) vs. Q^2 (Figure 3.5), after cooling to 250 K, the rate increases nearly linearly with Q^2, where the jump diffusion model applies, and the corresponding diffusion coefficient is 10.7±1.1 Å^2/ns (see Figure 3.5). After heating to 250 K, this rate becomes independent from Q for Q>1 Å(Figure 3.6).

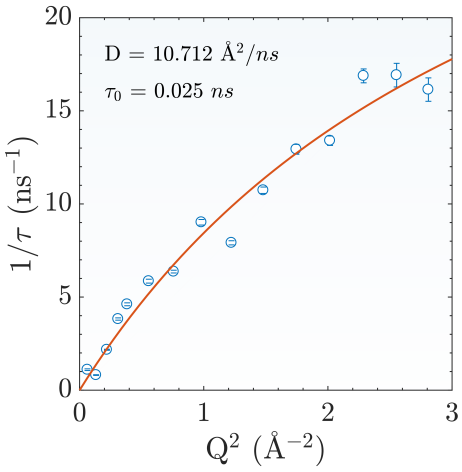

Figure 3.5: Molecular diffusion in the DBMMB electrolytes on cooling, assuming $\beta = 0.65$.

These results agree with our interpretation of the fixed-window scan of 1 M DBMMB. At 250 K, the Q-dependence after the cooling cycle is typical for a supercooled liquid (strong Q dependence), while heating to the same temperature results in mixed dynamics (weak Q dependence). This latter result suggests that the sample contains both liquid-like and solid-like microdomains, the latter resulting from burst nucleation after the cold crystallization prompted by heating. In other words, the two regions in Figure 3.6b have markedly different dynamics depending on whether the electrolyte is cooled or heated.

In the finding for high energy density electrolytes, using poorly packing, sterically frustrated ROMs like DBMMB is becoming increasingly popular for achieving high ROM solubility. For example, Shimizu et al. synthesized polyethylene oxide decorated quinone ROMs that were liquid at room temperature [62]. Takechi et al. used a methoxy-substituted stable TEMPO radical that formed eutectic mixtures with LiTFSI [63]. Cong et al. used a suitably modified ferrocene derivative [64]. Others have proposed using ionic liquids [65, 66], deep eutectic mixtures [67] and membrane-free cells containing immiscible solutions [68, 69] as possible approaches to increasing ROM concentration. One of the inherent dangers of operating flow cells in such high concentration regimes is that perturbation of solution properties by Ohmic heating and/or composition changes due to charging of ROMs can lead to phase separation that interferes with electrochemical cycling and flowing of energized fluids. The experiments described above demonstrate how small temperature changes near the phase transition temperature can cause burst crystallization from a metastable homogeneous solution. Our study shows that neutron scattering can become a sensitive diagnostic for the onset of such undesired conditions before they result in the electrochemically detectable loss of functionality.

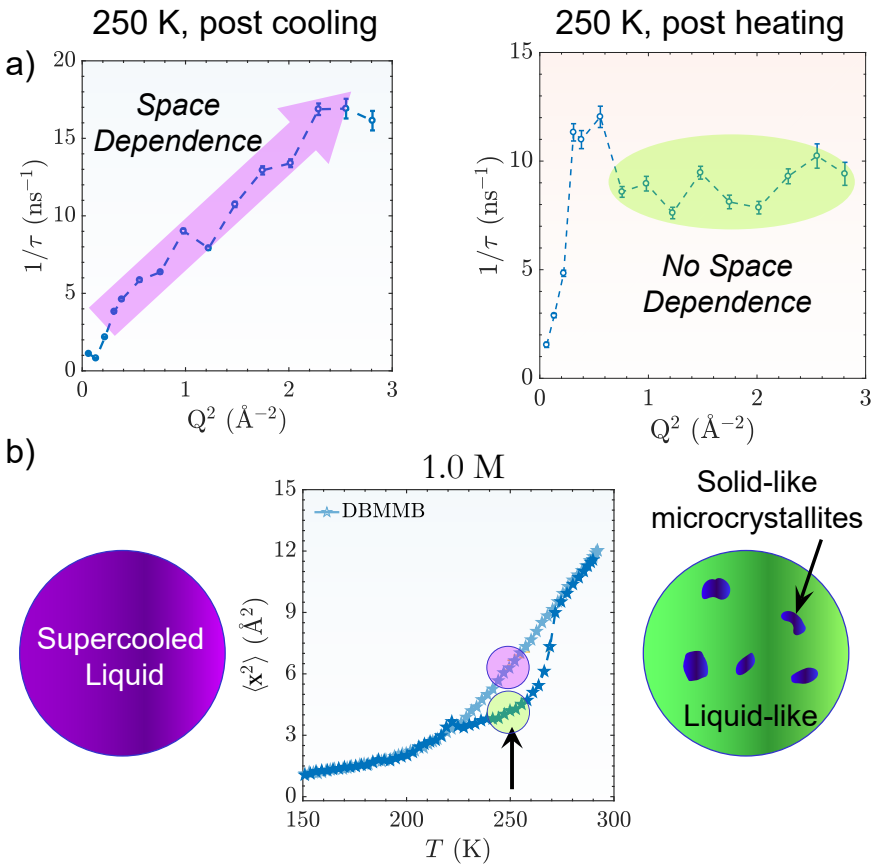

Figure 3.6: a) The supercooled solution of 1 M DBMMB at 250 K shows a parabolic Q dependence while only weak dependence of $1/\tau$ on Q is observed at 250 K after heating, suggesting mixed solid-like microcrystalline and liquid-like domains; b) cartoon denoting these regimes in the fixed-window scan.

Chapter 4

MD Simulations of LiTFSI Dissolved in Acetonitrile

As suggested in introduction and method sections, we hope to use MD simulation to predict properties of nonaqueous electrolyte solutions. Starting from a relative simple but significant model system: LiTFSI in acetonitrile, we optimized the force field and compared results using different force field. Neutron PDF and NMR were used to benchmark the force field.

4.1 Structural Properties Informed by MD Simulations and NPDF

As a first step in testing of the force fields, g(r) and S(k) functions were calculated. While g(r) is most sensitive to the local solvent structure, S(k) emphasizes structural correlations over longer distances. Figure 4.1a compares the computed S(k) with the NPDF data for a 1.5 M LiTFSI solution. The difference between the calculated traces is minor, indicating that all four force fields yield nearly identical solvent structures. At large k, shorter-range correlations contribute more to the oscillations seen in the traces. These perturbations include the length scales associated with the lithium ions. Due to their small ionic radii, these Li^+ cations interact strongly with the solvent molecules and $TFSI^-$ anions at short distances. The $TFSI^-$ anions screen electrostatic repulsion between the Li^+ ions, changing the Li^+-N (CH_3CN) and Li^+-O ($TFSI^-$) correlations seen in Figure 4.1a. The strong peak at 2 $Å^{-1}$ is mainly due to cation-cation, anion-anion, and solvent-solvent correlations. In Figure 4.1b, we show g(r) for interatomic distance r between 2 Å and 5 Å. When compared to our NPDF measurement, the MD simulations capture the main features, including the peaks at 1.1, 1.5, 1.8, and 2.05 Å, although their relative intensities are not well reproduced. The latter is due to the finite resolution of the instrument, spurious peaks introduced by numerical Fourier transform, and rigid structures for molecules and ions in the MD simulation.

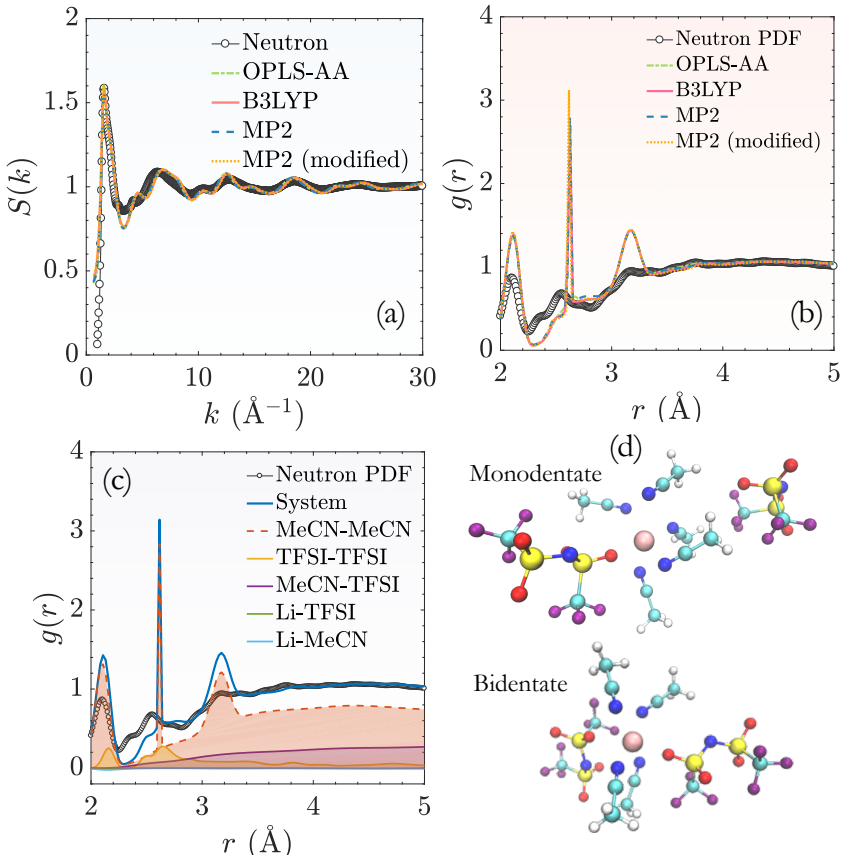

Figure 4.1: Structure factor from Neutron and MD simulation with different force field.

To separate contributions from different electrolyte components, g(r) can be decomposed into partial pair distribution function:

$$g(r) = \frac{\sum_{i,j} N_i N_j b_i b_j g_{i,j}(r)}{(\sum_i N_i b_i)^2} \tag{4.1}$$

where $g_{i,j}(r)$ is the partial PDF for a pair of species i and j, and b_i is the mean coherent neutron scattering length for N_i atoms in species i. Normalized coefficients in this equation give the relative weights for contributions from different pairs of electrolyte components (see Table 4.1).

Table 4.1: Computed weights for different pairs in neutron PDF (1.5 M LiTFSI in CD3CN)

Components	Coefficients
MeCN-MeCN	0.699
$TFSI^-$-$TFSI^-$	0.028
MeCN-$TFSI^-$	0.28
Li^+-$TFSI^-$	-0.006
Li^+-MeCN	-0.0012
Li^+-Li^+	0.000014

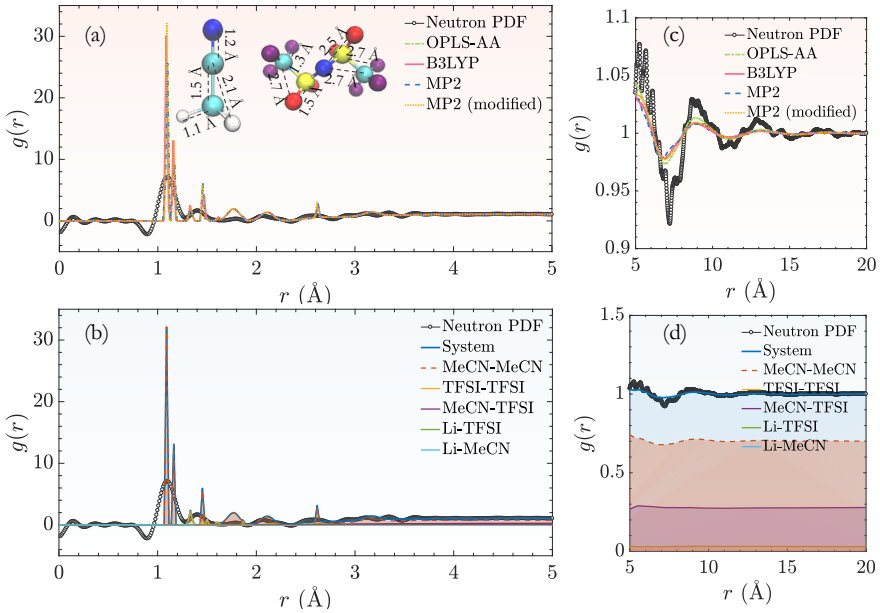

Figure 4.2: (a,c) Neutron PDF compared with g(r) calculated using different force fields at short (< 5 Å) and long distances (< 20 Å), respectively. (b,d) Experimental and calculated PDFs for different components obtained using MP2 force field.

Figure 4.1c shows a decomposition of the total PDF into such contributions for the MP2 force field. Since at 1.5 M LiTFSI the molar fraction of the salt is relatively low (∼ 9.1%). The main contribution to the total NPDF is from the solvent (∼ 70%). At short range, the C-C, C-H, and C-N bonds in the solvent are the main contribution. The peaks at 2.1 Å, 2.7 Å, and 3.2 Å are attributed to the first nearest neighbor correlations in the solvent molecules. Although the contribution of $TFSI^-$-$TFSI^-$ pairs is only 3%, it is observed due to the strong F-F peak at 2.2 Å and the C-N, S-F, C-O peaks at 2.7 Å. The contributions from Li^+TFSI^- and Li^+CD_3CN pairs are too small to observe (Table 4.1).

Figure 4.1d shows two representative solvation environments around the Li^+ ions. The main difference between them is in the coordination number of the Li^+ ion that interacts with one or two oxygens in $TFSI^-$ anions and several CN groups in the solvent molecules. Long range (> 5 Å) and short range (< 2 Å) data are shown in Figure 4.2. Once again, the differences among the four trial force fields are minor.

4.2 Dramatic Dynamics revealed by Diffusion Coefficient, and Electrical Conductivity

To quantify ionic diffusion in this electrolyte, mean squared displacements (MSDs) $\langle r^2 \rangle(t)$ for Li^+ and $TFSI^-$ ions were calculated using 100 ns MD trajectories. In the asymptotic regime (>10 ps), the MSD increases linearly with the time interval t as $6Dt$, where D is the diffusion coefficient. In Figures 4.3a and 4.3b, we compare the calculated MSD using our force fields and the NMR estimates (straight black lines in both panels) for 1.5 M LiTFSI. The first three force fields in Figures 4.3a and 4.3b yield ionic diffusivities that are around 10 times lower than our NMR estimates, signaling the problem discussed in the introduction.

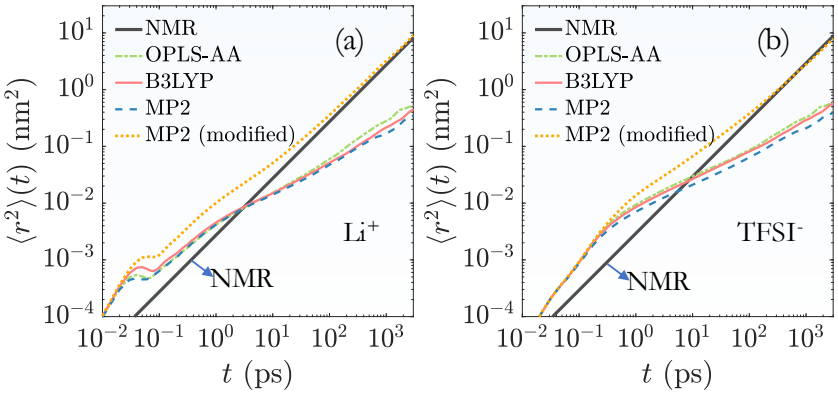

Figure 4.3: Mean squared displacement $\langle r^2 \rangle(t)$ for (a) Li^+ and (b) $TFSI^-$ ions calculated from our MD simulations for four different force fields (1.5 M LiTFSI/CD_3CN). The NMR measurement corresponds to the black straight line. The color-coding is the same as in Figures 4.1a and 4.1b.

Similar discrepancies have been reported for non-polarizable force fields used in MD simulation of ionic liquids [37][38]. Decreasing net charge on the ions [36][70] was suggested as a possible remedy. Inspired by these studies, we sought to establish whether the simplification works for traditional electrolytes. The major difference between these two systems is that ionic concentration is always high in the ionic liquids, and it is not given that decreasing charge applies over a wider range of ionic concentrations in a molecular solvent

(i.e., lower ionic conductivity). To implement this approach, the absolute ion charges were decreased to 0.8 a.u., and the atomic charges in $TFSI^-$ were scaled down accordingly. As seen in Figure 4.3, this relatively small modification considerably increases ionic diffusivity (so that MD estimates become consistent with our NMR measurements), while the simulated NPDF function does not change significantly (Figure 4.1).

In addition, we also calculated electrical conductivity using Green-Kubo relation by integrating electrical current correlation function [71, 72]:

$$\begin{aligned} \mathbf{J}(t) &= \sum_{i=1}^{N} q_i \mathbf{v}_i \\ \sigma &= \frac{1}{V k_B T} \int_0^\infty \langle \mathbf{J}(t) \cdot \mathbf{J}(0) \rangle dt \end{aligned} \tag{4.2}$$

where q_i is the molecular charge, $\mathbf{v}_i$ is the center of mass velocity, N is the total molecular number, $\mathbf{J}$ is the electrical current, and V is the volume of simulation box. The electrical current correlation function is shown in Fig 4.4 and the corresponding electrical conductivity is shown in Table 4.2 for different force fields.

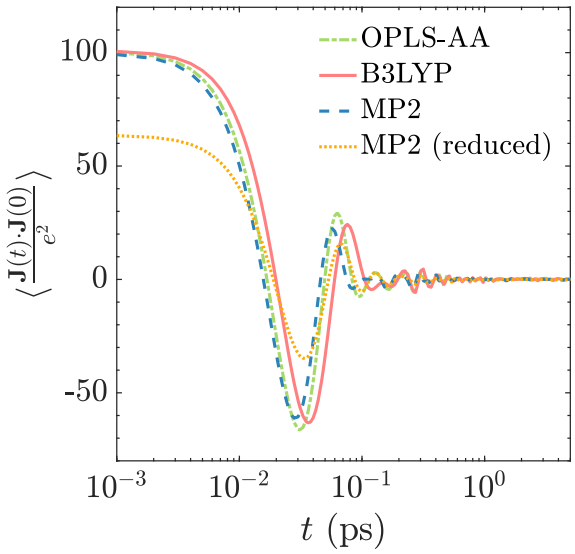

Figure 4.4: Electrical current correlation function, OPLS-AA (green dot dashed), B3LYP/6-31G(d) (pink solid), MP2/aug-cc-pVDZ (blue dashed), modified MP2/aug-cc-pVDZ (orange dotted).

Table 4.2: Computed electrical conductivity from MD using different force fields

FF	OPLS-AA	B3LYP	MP2	Modified MP2
σ (S/cm)	0.0063	0.0088	0.0046	0.022

From Table 4.2, the first three force fields predict electrical conductivity much smaller than reduced charge force field (modified MP2). The experimental measurement gives electrical conductivity as $\sigma_{exp} = 0.032$ (S/cm), which agrees well with modified MP2 calculation and confirms that different force fields predict different dynamics.

4.3 Concentration Dependence

To verify whether the scale-charge method works over a wider concentration range, we performed MD simulations at different concentrations of LiTFSI (0.2 M to 2 M). The comparison of calculated g(r) and S(k) with NPDFs at 0.5 and 1.0 M is given in Figures 4.5 and 4.6, respectively, while the corresponding diffusion coefficient is shown in Figure 4.6. The differences between the NPDFs computed using the four trial force fields were small, and they all agreed well with the experimental NPDFs. However, only the force field with reduced charges reproduced the experimental concentration dependencies of ionic diffusivity for [LiTFSI] $>$ 0.5 M, while the other force fields completely failed at these concentrations.

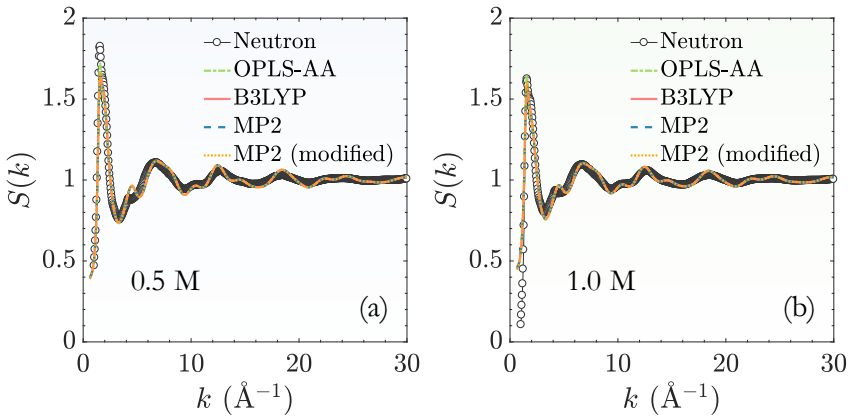

Figure 4.5: (a,b) Structure factors obtained from the NPDF experiment and MD simulations with different force fields for (a) 0.5 M LiTFSI and (b) 1.0 M LiTFSI solutions.

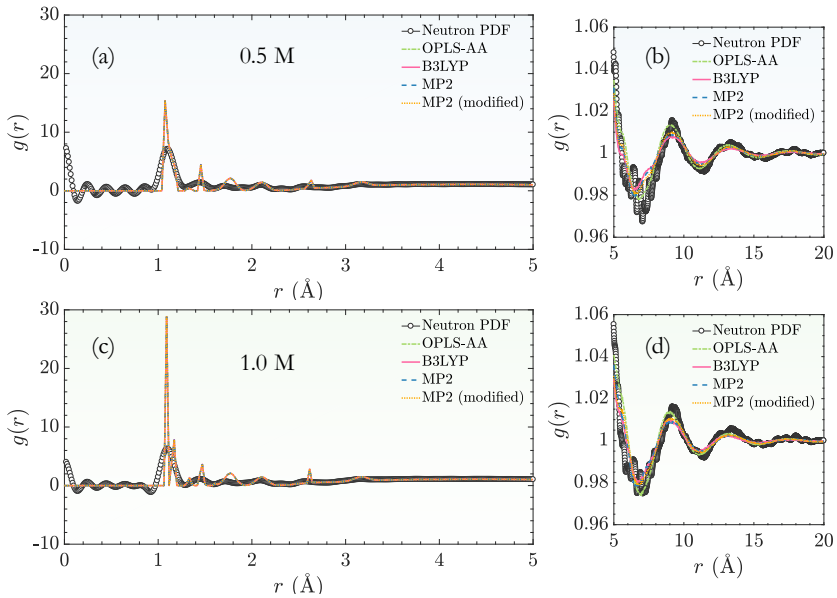

Figure 4.6: (a,c) Neutron PDF compared with g(r) calculated using different force fields at short (< 5 Å) and long distances (< 20 Å), respectively. (b,d) Experimental and calculated PDFs for different components obtained using MP2 force field.

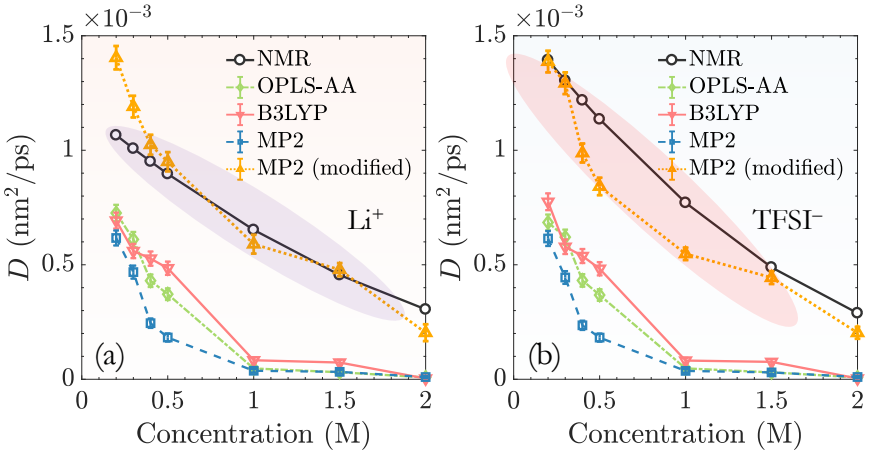

Figure 4.7: (a,b) Comparison of diffusion coefficients D for Li^+ and $TFSI^-$ ions in 0.2-2 M LiTFSI solutions in CD_3CN obtained in our NMR measurements (open circles) and MD simulations with different force fields. The color-coding is the same as in Figures 4.1 and 4.2.

4.4 The Explanation of the Same Structure but Different Dynamics: Energy Landscape

This method is rationalized using the free energy landscape shown in Figure 4.8. In this vast landscape, the valleys (local minima) are separated by ridges that frustrate thermally activated transitions between the minima. The degree of this frustration is determined by the balance of short-range and long-range forces in the system, which becomes a unique property for each force field. While almost identical local minima are given by all four force fields (i.e., the corresponding PDFs are similar), the barriers separating these minima are quite different in these models, resulting in different dynamic outcomes, with the reduced-charge force field giving the least frustration. Correcting the long-range interactions would require elaborate and computationally expensive force fields; the simplification circumvents this difficulty by reducing inter-valley barriers without changing the minima themselves. Our results suggest that the simplification works equally well for ionic liquids and sufficiently concentrated electrolytes that are based on molecular liquids, implying its broad generality.

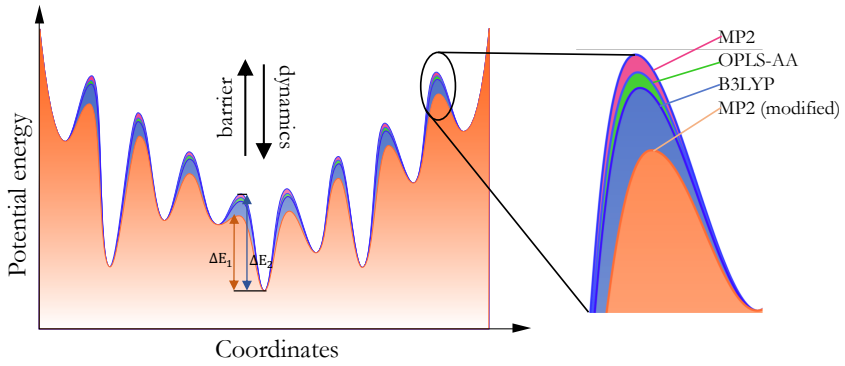

Figure 4.8: Schematic representations of energy landscape showing how different force fields predict similar minima but different barriers between minima.

In conclusion, refined force fields were used to compare MD simulations with neutron pair distribution functions (PDFs) and ionic diffusivity measurements in nonaqueous electrolytes. While all of the computed and experimental PDFs compare well, the computed diffusion coefficients for ions showed large deviations from our experimental estimates. By weakening the electrostatic interactions between these ions in the force field parameterization, we were able to obtain more realistic estimates for ionic diffusivities in 0.2-2 M LiTFSI$^-$$CD_3CN$ solutions without sacrificing the quality of the PDF simulation. Historically, the development of force fields for nonaqueous electrolytes focused mainly on solvation environments and short-range

properties (e.g., coordination numbers for ions). However, we caution that the resulting models can, and probably will, be inadequate to reproduce the dynamic properties of these electrolytes. As these properties are equally important for practical applications of these electrolytes, closer scrutiny and reassessment of force fields are required before in silico design of electrolyte systems can become predictive. Our study suggests that a surprisingly simple adjustment of these force fields (proportional scaling down of charges in the ions) can be used to reproduce the observed dynamic behaviors of ions in electrolytes over a wide concentration range with no effect on the computed PDF.

Chapter 5

Conclusions and Future Work

5.1 Conclusions

Nonaqueous electrolytes are important for many applications, especially for next generation batteries. Despite numerous existing studies, there are still many challenges in designing functional candidates due to strict requirement for those applications. To build a predictive model for nonaqueous electrolytes applied in nonaqueous redox flow battery, we applied neutron scattering measurements and MD simulations on several model systems. Specifically:

Neutron scattering has been used to probe the dynamics and phase behavior in complex functional fluids: concentrated electrolytes containing energy dense redox-active molecules. The electrolytes containing a catholyte molecule, DBMMB, showed the formation of surprisingly stable supercooled solutions and spontaneous crystallization on heating at 250 K. Our analyses indicate that slightly above this temperature the solution undergoes a spinodial decomposition into a mixture of solid-like and liquid-like domains, which causes slower translational diffusion of the catholyte molecule. Given that in the high concentration regimes such structural changes can readily occur due to charging and/or Ohmic heating of the electrolyte, we surmise that the ability of neutron scattering to detect the early onset of heterogeneity can be highly useful for the development of robust electrolyte systems for NRFBs.

Utilizing MD simulations, with quantum-mechanically refined force field, accompanied by neutron PDF and NMR measurements, we presented a detailed study of the structure and dynamics of a model nonaqueous electrolyte solution at molecular level. The structures characterized by the PDF of the system are consistent with the neutron PDF measurement for all force fields, which were usually considered as evidences of the validity of the simulations. However, the diffusion coefficients obtained from MD simulation exhibit dramatic differences among force fields even if the structures agree well with the experiments. Therefore, we conclude that matching the structure properties alone is not enough to benchmark a force field; dynamics must be also taken into consideration in the development of the force field of nonaqueous electrolyte solutions. These results suggest more rigorous scrutiny of the force fields used in the MD simulations is necessary for the

design and optimization of new electrolytes.

5.2 Future Work

We have not built a predictive model for nonaqueous electrolytes. In the future, we could do the following work to finish building the model:

• Study the concentration dependence of microheterogeneity by performing QENS on different concentrations of DBMMB-based nonaqueous electrolytes

In this thesis, we demonstrated that the microheterogeneity exists in crowded redox-active electrolytes. Due to time limitation, we only performed QENS measurement for 1 M DBMMB solutions. A direct follow-up will be whether microhetergeneity is present at lower concentration and what is the cross-over concentration? For redox flow battery, energy density is closely related with concentration. It will be interesting to see the concentration effect on the phase behavior and microscopic properties of nonaqueous electrolytes. On the other hand, it will help to optimize the concentration to avoid such adverse behavior.

• Perform $in-situ$ neutron scattering measurements to obtain real-time information during the cycling of NRFBs

At this stage, all the neutron scattering we have performed were just the static mixture of supporting electrolyte, anolyte, and catholyte, which is highly simplified compared to a real battery system. In reality, there will be electrical current applied to the battery during the cycling. The high chemical activity of NRFBs makes the battery very sensitive to the operating conditions and results in a significant materials interaction, which requires a systematic investigation of the battery under real operation conditions. In addition, neutron scattering is a non-destructive technique, making neutron scattering appropriate for $in-situ$ measurements.

• Apply developed force field to solutions, including DBMMB-based and DMB-based nonaqueous electrolytes

In the MD simulation part of this thesis, we found that structure alone is not enough for benchmarking a force field, dynamical properties matters, too. By scaling the charge based on the quantum-chemically parameterized force field, both structures and dynamics agree well with experimental measurements. To this end, we could perform similar quantum chemistry calculations for DBMMB, DMB, and BzNSN to develop accurate force field. Then using developed force field, we can perform MD simulations on the solutions to explore the structural and dynamical characteristics of these nonaqueous electrolytes.

References

[1] Song Li, Guang Feng, Pasquale F. Fulvio, Patrick C. Hillesheim, Chen Liao, Sheng Dai, and Peter T. Cummings. Molecular dynamics simulation study of the capacitive performance of a binary mixture of ionic liquids near an onion-like carbon electrode. *Journal of Physical Chemistry Letters*, 3(17):2465–2469, 2012.

[2] Maxim V. Fedorov and Alexei A. Kornyshev. Ionic liquids at electrified interfaces. *Chemical Reviews*, 114(5):2978–3036, 2014.

[3] J B Goodenough, H. D. Abruna, and M. V. Buchanan. Basic Research Needs for Electrical Energy Storage. Report of the Basic Energy Sciences Workshop on Electrical Energy Storage, April 2-4, 2007. page 186, apr 2007.

[4] Przemyslaw Kubisa. Application of ionic liquids as solvents for polymerization processes. *Progress in Polymer Science (Oxford)*, 29(1):3–12, 2004.

[5] Fikile R. Brushett, John T. Vaughey, and Andrew N. Jansen. An all-organic non-aqueous lithium-ion redox flow battery. *Advanced Energy Materials*, 2(11):1390–1396, 2012.

[6] Jan Winsberg, Tino Hagemann, Tobias Janoschka, Martin D. Hager, and Ulrich S. Schubert. Redox-Flow Batteries: From Metals to Organic Redox-Active Materials. *Angewandte Chemie - International Edition*, 56(3):686–711, 2017.

[7] Grigorii L. Soloveichik. Flow Batteries: Current Status and Trends. *Chemical Reviews*, 115(20):11533–11558, 2015.

[8] Wei Wang, Qingtao Luo, Bin Li, Xiaoliang Wei, Liyu Li, and Zhenguo Yang. Recent progress in redox flow battery research and development. *Advanced Functional Materials*, 23(8):970–986, 2013.

[9] Liyu Li, Soowhan Kim, Wei Wang, M. Vijayakumar, Zimin Nie, Baowei Chen, Jianlu Zhang, Guanguang Xia, Jianzhi Hu, Gordon Graff, Jun Liu, and Zhenguo Yang. A stable vanadium redox-flow battery with high energy density for large-scale energy storage. *Advanced Energy Materials*, 1(3):394–400, 2011.

[10] Piergiorgio Alotto, Massimo Guarnieri, and Federico Moro. Redox flow batteries for the storage of renewable energy: A review. *Renewable and Sustainable Energy Reviews*, 29:325–335, 2014.

[11] Ke Gong, Qianrong Fang, Shuang Gu, Sam Fong Yau Li, and Yushan Yan. Nonaqueous redox-flow batteries: Organic solvents, supporting electrolytes, and redox pairs. *Energy and Environmental Science*, 8(12):3515–3530, 2015.

[12] Babu R. Chalamala, Thiagarajan Soundappan, Graham R. Fisher, Mitchell R. Anstey, Vilayanur V. Viswanathan, and Michael L Perry. Redox Flow Batteries: An Engineering Perspective. *Proceedings of the IEEE*, 102(6):976–999, jun 2014.

[13] Robert M. Darling, Kevin G. Gallagher, Jeffrey A. Kowalski, Seungbum Ha, and Fikile R. Brushett. Pathways to low-cost electrochemical energy storage: A comparison of aqueous and nonaqueous flow batteries. *Energy and Environmental Science*, 7(11):3459–3477, 2014.

[14] Kang Xu. Nonaqueous liquid electrolytes for lithium-based rechargeable batteries. *Chemical Reviews*, 104(10):4303–4417, 2004.

[15] L. Su, M. Ferrandon, J. A. Kowalski, J. T. Vaughey, and F. R. Brushett. Electrolyte Development for Non-Aqueous Redox Flow Batteries Using a High-Throughput Screening Platform. *Journal of the Electrochemical Society*, 161(12):A1905–A1914, 2014.

[16] Lu Zhang, Zhengcheng Zhang, Paul C. Redfern, Larry A. Curtiss, and Khalil Amine. Molecular engineering towards safer lithium-ion batteries: A highly stable and compatible redox shuttle for overcharge protection. *Energy and Environmental Science*, 5(8):8204–8207, 2012.

[17] Jinhua Huang, Lei Cheng, Rajeev S. Assary, Peiqi Wang, Zheng Xue, Anthony K. Burrell, Larry A. Curtiss, and Lu Zhang. Liquid catholyte molecules for nonaqueous redox flow batteries. *Advanced Energy Materials*, 5(6):1–6, 2015.

[18] Xiaoliang Wei, Wu Xu, Jinhua Huang, Lu Zhang, Eric Walter, Chad Lawrence, M. Vijayakumar, Wesley A. Henderson, Tianbiao Liu, Lelia Cosimbescu, Bin Li, Vincent Sprenkle, and Wei Wang. Radical Compatibility with Nonaqueous Electrolytes and Its Impact on an All-Organic Redox Flow Battery. *Angewandte Chemie - International Edition*, 54(30):8684–8687, 2015.

[19] Wentao Duan, Jinhua Huang, Jeffrey A. Kowalski, Ilya A. Shkrob, M. Vijayakumar, Eric Walter, Baofei Pan, Zheng Yang, Jarrod D. Milshtein, Bin Li, Chen Liao, Zhengcheng Zhang, Wei Wang, Jun Liu, Jeffery S. Moore, Fikile R. Brushett, Lu Zhang, and Xiaoliang Wei. "wine-dark sea" in an organic flow battery: Storing negative charge in 2,1,3-benzothiadiazole radicals leads to improved cyclability. *ACS Energy Letters*, 2(5):1156–1161, 2017.

[20] Jinhua Huang, Wentao Duan, Jingjing Zhang, Ilya A. Shkrob, Rajeev S. Assary, Baofei Pan, Chen Liao, Zhengcheng Zhang, Xiaoliang Wei, and Lu Zhang. Substituted thiadiazoles as energy-rich anolytes for nonaqueous redox flow cells. *Journal of Materials Chemistry A*, 6(15):6251–6254, 2018.

[21] Yasuo Kameda, Yasuhiro Umebayashi, Munetaka Takeuchi, Mohanmmad Abdul Wahab, Shuhei Fukuda, Shin Ichi Ishiguro, Motoya Sasaki, Yuko Amo, and Takeshi Usuki. Solvation structure of Li+ in concentrated LiPF 6-propylene carbonate solutions. *Journal of Physical Chemistry B*, 111(22):6104–6109, 2007.

[22] Daniel M. Seo, Oleg Borodin, Sang-Don Han, Quang Ly, Paul D. Boyle, and Wesley A. Henderson. Electrolyte Solvation and Ionic Association. *Journal of The Electrochemical Society*, 159(5):A553, 2012.

[23] Xuedan Song, Hiroshi Hamano, Babak Minofar, Ryo Kanzaki, Kenta Fujii, Yasuo Kameda, Shinji Kohara, Masayoshi Watanabe, Shin Ichi Ishiguro, and Yasuhiro Umebayashi. Structural heterogeneity and unique distorted hydrogen bonding in primary ammonium nitrate ionic liquids studied by high-energy X-ray diffraction experiments and MD simulations. *Journal of Physical Chemistry B*, 116(9):2801–2813, mar 2012.

[24] Jeevapani J. Hettige, Juan Carlos Araque, and Claudio J. Margulis. Bicontinuity and multiple length scale ordering in triphilic hydrogen-bonding ionic liquids. *Journal of Physical Chemistry B*, 118(44):12706–12716, 2014.

[25] G. L. Squires. *Introduction to the Theory of Thermal Neutron Scattering*. Cambridge University Press, 3 edition, 2012.

[26] Zi-Fa Shi, Hayden T Black, Afshin Dadvand, and Dmitrii F Perepichka. Pentacenobis(thiadiazole)dione, an n-Type Semiconductor for Field-Effect Transistors. *J. Org. Chem*, 79, 2014.

[27] Nobuhiro Ito, Hiroyoshi Esaki, Tsuneaki Maesawa, Eikoh Imamiya, Tomohiro Maegawa, and Hironao Sajiki. Efficient and selective Pt/C-catalyzed H-D exchange reaction of aromatic rings. *Bulletin of the Chemical Society of Japan*, 81(2):278–286, 2008.

[28] Jörg Neuefeind, Mikhail Feygenson, John Carruth, Ron Hoffmann, and Kenneth K Chipley. The Nanoscale Ordered MAterials Diffractometer NOMAD at the Spallation Neutron Source SNS. *Nuclear Instruments and Methods in Physics Research Section B: Beam Interactions with Materials and Atoms*, 287:68–75, sep 2012.

[29] WS Price. Pulsed-field gradient nuclear magnetic resonance as a tool for studying translational diffusion: Part 1. Basic theory. *Concepts Magn. Reson.*, 9:299–336, 1998.

[30] C S Johnson Jr. Diffusion ordered nuclear magnetic resonance spectroscopy: principles and applications. *Progress in Nuclear Magnetic Resonance Spectroscopy*, 34:203–256, 1999.

[31] Oleg Borodin. Polarizable force field development and molecular dynamics simulations of ionic liquids. *Journal of Physical Chemistry B*, 113(33):11463–11478, 2009.

[32] Shu Li, Zhen Cao, Yuxing Peng, Lei Liu, Vonglong Wang, Shu Wang, Ji Qiang Wang, Tianying Yan, Xue Ping Gao, De Ying Song, and Pan Wen Shen. Molecular dynamics simulation of LiTFSI-acetamide electrolytes: Structural properties. *Journal of Physical Chemistry B*, 112(20):6398–6410, may 2008.

[33] Volker Lesch, Zhe Li, Dmitry Bedrov, Oleg Borodin, and Andreas Heuer. The influence of cations on lithium ion coordination and transport in ionic liquid electrolytes: a MD simulation study. *Phys. Chem. Chem. Phys.*, 18(1):382–392, 2016.

[34] William L. Jorgensen, David S. Maxwell, and Julian Tirado-Rives. Development and testing of the OPLS all-atom force field on conformational energetics and properties of organic liquids. *Journal of the American Chemical Society*, 118(45):11225–11236, 1996.

[35] Somisetti V. Sambasivarao and Orlando. Acevedo. Development of OPLS-AA Force Field Parameters for 68 Unique Ionic Liquids. *Journal of Chemical Theory and Computation*, 5(4):1038–1050, apr 2009.

[36] B. L. Bhargava and S. Balasubramanian. Refined potential model for atomistic simulations of ionic liquid [bmim] [P F6]. *Journal of Chemical Physics*, 127(11), 2007.

[37] Thorsten Köddermann, Dietmar Paschek, and Ralf Ludwig. Molecular dynamic simulations of ionic liquids: A reliable description of structure, thermodynamics and dynamics. *ChemPhysChem*, 8(17):2464–2470, 2007.

[38] Jan Picálek and Jií Kolafa. Molecular dynamics study of conductivity of ionic liquids: The Kohlrausch law. *Journal of Molecular Liquids*, 134(1-3 SPEC. ISS.):29–33, 2007.

[39] Oleg Borodin, W. Gorecki, Grant D. Smith, and Michel Armand. Molecular dynamics simulation and pulsed-field gradient NMR studies of Bis(fluorosulfonyl)imide (FSI) and Bis[(trifluoromethyl)sulfonyl]imide (TFSI)-based ionic liquids. *Journal of Physical Chemistry B*, 114(20):6786–6798, 2010.

[40] Yuki Yamada, Keizo Furukawa, Keitaro Sodeyama, Keisuke Kikuchi, Makoto Yaegashi, Yoshitaka Tateyama, and Atsuo Yamada. Unusual stability of acetonitrile-based superconcentrated electrolytes for fast-charging lithium-ion batteries. *Journal of the American Chemical Society*, 136(13):5039–5046, 2014.

[41] F. Martin and H. Zipse. Charge distribution in the water molecule -A comparison of methods. *Journal of Computational Chemistry*, 26(1):97–105, 2005.

[42] M. J. Frisch, G. W. Trucks, H. B. Schlegel, G. E. Scuseria, M. A. Robb, J. R. Cheeseman, G. Scalmani, V. Barone, G. A. Petersson, H. Nakatsuji, X. Li, M. Caricato, A. V. Marenich, J. Bloino, B. G. Janesko, R. Gomperts, B. Mennucci, H. P. Hratchian, J. V. Ortiz, A. F. Izmaylov, J. L. Sonnenberg, D. Williams-Young, F. Ding, F. Lipparini, F. Egidi, J. Goings, B. Peng, A. Petrone, T. Henderson, D. Ranasinghe, V. G. Zakrzewski, J. Gao, N. Rega, G. Zheng, W. Liang, M. Hada, M. Ehara, K. Toyota, R. Fukuda, J. Hasegawa, M. Ishida, T. Nakajima, Y. Honda, O. Kitao, H. Nakai, T. Vreven, K. Throssell, J. A.

Montgomery, Jr., J. E. Peralta, F. Ogliaro, M. J. Bearpark, J. J. Heyd, E. N. Brothers, K. N. Kudin, V. N. Staroverov, T. A. Keith, R. Kobayashi, J. Normand, K. Raghavachari, A. P. Rendell, J. C. Burant, S. S. Iyengar, J. Tomasi, M. Cossi, J. M. Millam, M. Klene, C. Adamo, R. Cammi, J. W. Ochterski, R. L. Martin, K. Morokuma, O. Farkas, J. B. Foresman, and D. J. Fox. Gaussian09 Revision D.01, 2016. Gaussian Inc. Wallingford CT.

[43] Curt M. Breneman and Kenneth B. Wiberg. Determining atomcentered monopoles from molecular electrostatic potentials. the need for high sampling density in formamide conformational analysis. *Journal of Computational Chemistry*, 11(3):361–373, 4 1990.

[44] Seiji Tsuzuki, Wataru Shinoda, Md. Shah Miran, Hiroshi Kinoshita, Tomohiro Yasuda, and Masayoshi Watanabe. Interactions in ion pairs of protic ionic liquids: Comparison with aprotic ionic liquids. *The Journal of Chemical Physics*, 139(17):174504, nov 2013.

[45] H. J.C. Berendsen, D. van der Spoel, and R. van Drunen. GROMACS: A message-passing parallel molecular dynamics implementation. *Computer Physics Communications*, 91(1-3):43–56, 1995.

[46] Erik Lindahl, Berk Hess, and David van der Spoel. GROMACS 3.0: A package for molecular simulation and trajectory analysis, 2001.

[47] David Van Der Spoel, Erik Lindahl, Berk Hess, Gerrit Groenhof, Alan E. Mark, and Herman J.C. Berendsen. GROMACS: Fast, flexible, and free, 2005.

[48] Berk Hess, Carsten Kutzner, David Van Der Spoel, and Erik Lindahl. GRGMACS 4: Algorithms for highly efficient, load-balanced, and scalable molecular simulation. *Journal of Chemical Theory and Computation*, 4(3):435–447, 2008.

[49] Claudia Steffen, Klaus Thomas, Uwe Huniar, Arnim Hellweg, Oliver Rubner, and Alexander Schroer. TmoleX-A graphical user interface for TURBOMOLE. *Journal of Computational Chemistry*, 31(16):n/a–n/a, aug 2010.

[50] Nathan P. Walter, Abhishek Jaiswal, Zhikun Cai, and Yang Zhang. LiquidLib: A comprehensive toolbox for analyzing classical and ab initio molecular dynamics simulations of liquids and liquid-like matter with applications to neutron scattering experiments. *Computer Physics Communications*, 228:209–218, jul 2018.

[51] Ryogo Kubo. Stochastic Liouville equations. *Journal of Mathematical Physics*, 4(2):174–183, 1963.

[52] Ke Yang, Madhusudan Tyagi, and Yang Zhang. Odd Even Glass Transition Temperatures in Network-Forming Ionic. 2013.

[53] Denis A. Bashirov, Taisiya S. Sukhikh, Natalia V. Kuratieva, Elena A. Chulanova, Irina V. Yushina, Nina P. Gritsan, Sergey N. Konchenko, and Andrey V. Zibarev. Novel applications of functionalized 2,1,3-benzothiadiazoles for coordination chemistry and crystal engineering. *RSC Advances*, 4(54):28309–28316, 2014.

[54] Anthony F. Cozzolino, Ignacio Vargas-Baca, Sarah Mansour, and Amir H. Mahmoudkhani. The nature of the supramolecular association of 1,2,5-chalcogenadiazoles. *Journal of the American Chemical Society*, 127(9):3184–3190, 2005.

[55] Mark S. Searle and Dudley H. Williams. The Cost of Conformational Order: Entropy Changes in Molecular Associations. *Journal of the American Chemical Society*, 114(27):10690–10697, 1992.

[56] M. Choy De Martinez, O. P. Márquez, J. Márquez, F. Hahn, B. Beden, P. Crouigneau, A. Rakotondrainibe, and C. Lamy. In situ spectroscopic investigation of the anodic oxidation of 1,4-dimethoxybenzene at platinum electrodes. *Synthetic Metals*, 88(3):187–196, 1997.

[57] Jingjing Zhang, Zheng Yang, Ilya A. Shkrob, Rajeev S. Assary, Siu on Tung, Benjamin Silcox, Wentao Duan, Junjie Zhang, Chi Cheung Su, Bin Hu, Baofei Pan, Chen Liao, Zhengcheng Zhang, Wei Wang, Larry A. Curtiss, Levi T. Thompson, Xiaoliang Wei, and Lu Zhang. Annulated Dialkoxybenzenes as Catholyte Materials for Non-aqueous Redox Flow Batteries: Achieving High Chemical Stability through Bicyclic Substitution. *Advanced Energy Materials*, 7(21):1–5, 2017.

[58] Zonghai Chen and K. Amine. Degradation pathway of 2,5-di-tert-butyl-1,4-dimethoxybenzene at high potential. *Electrochimica Acta*, 53(2):453–458, 2007.

[59] K. S. Singwi and A. Sjölander. Resonance absorption of nuclear gamma rays and the dynamics of atomic motions. *Phys. Rev.*, 120:1093–1102, Nov 1960.

[60] C T Chudley and R J Elliott. Neutron scattering from a liquid on a jump diffusion model. *Proceedings of the Physical Society*, 77(2):353, 1961.

[61] Yang Zhang, Marco Lagi, Dazhi Liu, Francesco Mallamace, Emiliano Fratini, Piero Baglioni, Eugene Mamontov, Mark Hagen, and Sow-Hsin Chen. Experimental evidence of fragile-to-strong dynamic crossover in DNA hydration water. *The Journal of Chemical Physics*, 130:215103, 2009.

[62] Akihiro Shimizu, Keisuke Takenaka, Naoyuki Handa, Toshiki Nokami, Toshiyuki Itoh, and Jun Ichi Yoshida. Liquid Quinones for Solvent-Free Redox Flow Batteries. *Advanced Materials*, 29(41):1–5, 2017.

[63] Kensuke Takechi, Yuichi Kato, and Yoko Hase. A highly concentrated catholyte based on a solvate ionic liquid for rechargeable flow batteries. *Advanced Materials*, 27(15):2501–2506, 2015.

[64] Guangtao Cong, Yucun Zhou, Zhejun Li, and Yi Chun Lu. A highly concentrated catholyte enabled by a low-melting-point ferrocene derivative. *ACS Energy Letters*, 2(4):869–875, 2017.

[65] Tao Gao, Xiaogang Li, Xiwen Wang, Junkai Hu, Fudong Han, Xiulin Fan, Liumin Suo, Alex J. Pearse, Sang Bok Lee, Gary W. Rubloff, Karen J. Gaskell, Malachi Noked, and Chunsheng Wang. A Rechargeable Al/S Battery with an Ionic-Liquid Electrolyte. *Angewandte Chemie - International Edition*, 55(34):9898–9901, 2016.

[66] Ruiyong Chen and Rolf Hempelmann. Ionic liquid-mediated aqueous redox flow batteries for high voltage applications. *Electrochemistry Communications*, 70:56–59, 2016.

[67] J. C. Goeltz and L. N. Matsushima. Metal-free redox active deep eutectic solvents. *Chemical Communications*, 53(72):9983–9985, 2017.

[68] Musbaudeen O. Bamgbopa, Yang Shao-Horn, Raed Hashaikeh, and Saif Almheiri. Cyclable membraneless redox flow batteries based on immiscible liquid electrolytes: Demonstration with all-iron redox chemistry. *Electrochimica Acta*, 267:41–50, 2018.

[69] Paula Navalpotro, Jesus Palma, Marc Anderson, and Rebeca Marcilla. A Membrane-Free Redox Flow Battery with Two Immiscible Redox Electrolytes. *Angewandte Chemie - International Edition*, 56(41):12460–12465, 2017.

[70] Florian Dommert, Katharina Wendler, Robert Berger, Luigi Delle Site, and Christian Holm. Force fields for studying the structure and dynamics of ionic liquids: A critical review of recent developments. *ChemPhysChem*, 13(7):1625–1637, 2012.

[71] Aris Marcolongo and Nicola Marzari. Ionic correlations and failure of Nernst-Einstein relation in solid-state electrolytes. *PHYSICAL REVIEW MATERIALS*, 1:25402, 2017.

[72] C. Schröder, M. Haberler, and O. Steinhauser. On the computation and contribution of conductivity in molecular ionic liquids. *Journal of Chemical Physics*, 128(13), 2008.